CHALMERS

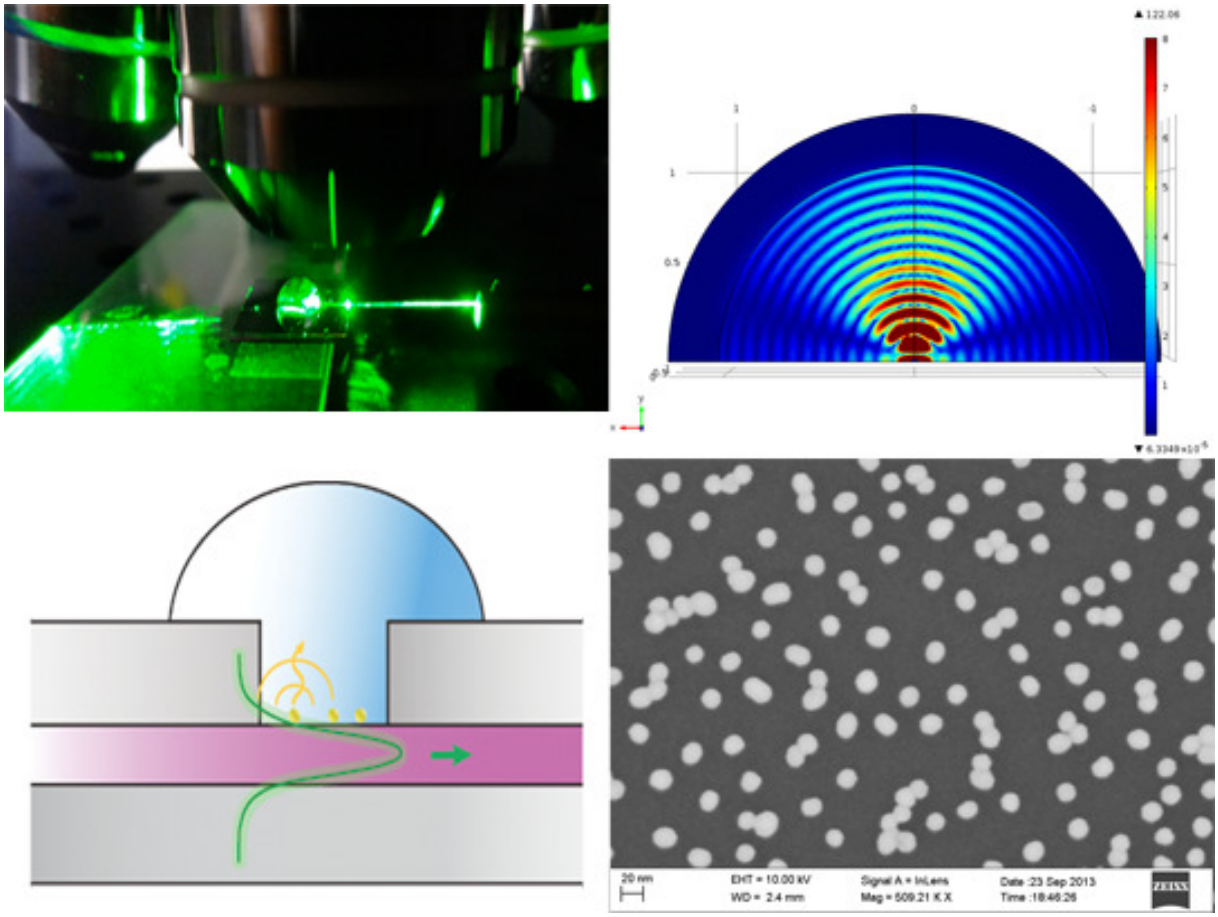

# Scattering of gold nanoparticles in an evanescent waveguide field

*Master's Thesis in Applied Physics*

MARTIN KARLBERG

Department of Applied Physics
Division of Biological Physics
Chalmers University of Technology
Gothenburg, Sweden 2013

THESIS FOR THE DEGREE OF MASTER OF SCIENCE

# Scattering of gold nanoparticles in an evanescent waveguide field

MARTIN KARLBERG


CHALMERS

Department of Applied Physics
CHALMERS UNIVERSITY OF TECHNOLOGY
Gothenburg, Sweden 2013

**Scattering of gold nanoparticles in an evanescent waveguide field**

MARTIN KARLBERG



Department of Applied Physics
*Division of Biological Physics*
Chalmers University of Technology
SE-412 96 Gothenburg
Sweden
Telephone +46(0)31-772 10 00

Printed at Chalmers Reproservice Gothenburg, 2013

Cover illustration: *The front page consists of four illustrations. The top-left is a symbol for experimental work. It pictures the microscope device where the laser fibre is aligned with the waveguide chip. Top-right is a symbol for the simulation work. The figure demonstrate how a gold nanoparticle will scatter incoming light of a plane wave. Bottom-left is a symbol of theory. The figure describes how a light mode will propagate in the waveguide and give rise to scatter when interacting with gold nanoparticles. Bottom-right is a symbol of reference methods. It is a picture of gold nanoparticles taken from a scanning electron microscope.*

Scattering of gold nanoparticles in an evanescent waveguide field

MARTIN KARLBERG
Department of Applied Physics
*Division of Biological Physics*
Chalmers University of Technology
Gothenburg, Sweden 2013

# Abstract

Biomedicine aims at the development of improvement of medical care. One aspect of this aim is the early detection of the onset of disease. In this thesis, single molecule detection by optical waveguides has been used for the detection of low concentration of substances, a method that could be useful for the early discovery of diseases or harmful substances in the body. As such techniques are not yet optimised, this thesis presents a further analyse of such setups.

It is of importance to catch sight of the disease as early as possible in order to be able to delay or cure it. Single molecule detection by optical waveguides is a method for detection of low concentrations of substances which could be useful in the early discovery of diseases or harmful substances in your body. The technique is not yet optimised and it is therefore required that it is analysed more into detail before it can be used reliably.

The first part of this thesis explains the theory behind optical waveguides and the formation of modes within them and also the scattering process of nanoparticles situated in their evanescent field. The second part of the thesis investigates if it is possible to simulate gold nanoparticles in a waveguide's evanescent field to observe and map how they scatter. COMSOL Multiphysics was used for this type of simulation. The last part explains the experimental efforts made to optimise the method of particle detection using the waveguide platform.

The conclusion is that the technique of single molecule detection through scattering on waveguides is a useful method for bio-related applications. It is furthermore concluded that it is possible through scatter measurements to determine the size of different particles immobilised on the waveguide surface, if there are known particles of reference. This area of research should be studied further, as there could be a plethora of application areas, chiefly within biomedicine.

**Keywords:** nanoparticles, optical modes, scattering, single molecule detection, waveguides.

## Acknowledgements

With these words I would like to thank the persons who have supported me when working with this thesis. I owe a debt of gratitude to:

**Mattias Marklund** my supervisor and examiner. Thank you for being available and always positive. It has been nice to work with you and to have someone to share ideas with and to consult when problems have arisen.

**Björn Agnarsson** for all help, availability and the never ending interest and engagement in me and my project. You have really helped me a lot. Thank you.

**Fredrik Höök** Thank for giving me the idea to this project and the opportunity to work in your research group. Your enthusiasm has rubbed off on me.

**Mathias Elmeskog** for all help and support. You have always been available and ready to answer questions and to help me with practical things.

**Anders Lundgren** for helping me with the fabrication and size determination of the gold particles.

**Biological Physics Group** for being nice to me and always being ready to answer questions.

**Comsol support** Thank you Daniel Ericsson, Linus Andersson, Ulf Olin and Reine Granström for your competence and your answers.

**Igor Zorić** my mentor at Chalmers. Thank you for the advice you have given me and the interesting talks we have had.

**Friends** Thank you Björn Johansson and Emma Andersson for helping me with LaTeXand thank you Nicolas Wolf for proofreading my report.

**Family** for the support and care you have shown, helping me to the point where I am today. And thank you Nina for the understanding you have shown towards me and for taking care of me in hard times.

Martin Karlberg, Gothenburg, 10 October 2013

# Contents

# 1
# Introduction

In much of the biological and physical research today it is of great important to be able to detect and measure micro- and nano sized objects. This is often done by labelling the samples with e.g. fluorophores. But when using labels, one has to take into account that the labels themselves may influence, or be influenced by, the specimen during the experiment. It can also be a problem to evenly distribute the labels over the specimen. In such cases it would be preferred to be able to detect and measure single particles or molecules without the use of fluorophore labels. This can be done by evanescent-field waveguides. These types of waveguides will support electromagnetic modes that will scatter if they interact with matter on the waveguide surface.

Gold nanoparticles have a great ability to scatter light, which makes them an ideal tool to study light-matter interactions on waveguides. The gold nanoparticles can therefore be used to label biological molecules. The research group together with which these experiments have been carried out has, among other qualities, great competence when it comes to characterisation and size control of gold nanoparticles. This thesis will cover some theoretical and experimental work done to investigate the use gold nanoparticles as scatterers on planar waveguides.

## 1.1 Introduction to optical waveguides

Total internal reflection-based optical waveguides are used to detect and investigate nanoparticles in the proximity to the interface between the waveguide surface and the substrate within which the nanoparticles of interest are situated. Such setups are of great diagnostic importance, and have a multitude of applications. However, the geometry and field configuration in such setups are often rather complex. The close collaboration between experimental and theoretical efforts that this thesis provides may help to deepen the understanding of these systems and applications thereof. A deeper view into the structure and physics behind evanescent-field waveguides is given in chapters 2 and 3.

The use of waveguides is not yet optimised. Some of the problems connected to labeling microscopy still remain. One of these problems concerns how to quantify the data measured. All measurements will vary from one another due to the human factor, the humidity in the room etcetera. If the measuring technique using evanescent-field optical waveguides is to be extensively used within the industry, it is important to decide and optimise the parameters of the system.

## 1.2 Scope

As mentioned above, one question concerns how to quantify the data being measured. One purpose of this thesis was to find out how different parameters may affect the measurements. This thesis will demonstrate ways that can be used to find out about the influence of these parameters. At first there will be a theoretical summation of the physics being the basis of the waveguide measuring technique in chapter 2. Chapter 3 will then cover the methods used and in chapters 5 and 6 there will be a discussion about what has been done and what can be further done in the future.

As a way to numerically visualise, quantify and make predictions of the nanoparticle measurements, COMSOL Multiphysics (hereafter referred to as Comsol) has been used. These simulations were made as a first step to recreate the optical modal field that arises within the waveguide when it is in use. As a second step, the simulations were going to predict how the evanescent field of the waveguide would scatter when interacting with gold nanoparticles.

Gold nanoparticles have some favourable properties making them suitable for experimental work. First of all they are chemically inert and therefore not toxic. Moreover they can be functionalised, they show monodisperse size distribution as well as they are good scatterers. The last property has a large significance to this thesis.

To validate the results from the simulations, they have been compared to theory. Corresponding experiments were also performed. The aim of the experimental work was to improve the waveguide scattering detection method by looking at many different parameters of the system and decide if they could be changed or optimised. Another item of interest was to see whether intensity measurements from the waveguide scattering could be used to determine the size of the particles bound to its surface.

An interesting feature of the scattering system is that gold nanoparticles as small as around 65 nm clearly can be seen by putting an iPhone 5 (from now on referred to as the mobile phone) to the ocular of the microscope. In the future this feature hopefully can connect the world of research with the real application.

# 2
# Theoretical background

## 2.1 Maxwell's equations

THIS SECTION AIMS to give the reader a background knowledge in the fundamental optical properties required to understand the mechanisms utilised in this thesis.

### 2.1.1 Plane waves in a nonconducting medium

The most basic propagating electromagnetic waves are the plane waves. In the case of an infinite, nonconducting dielectric media with isotropic permeability and susceptibility the plane waves can be described by Maxwell's equations:

$$\begin{aligned} \nabla \cdot \mathbf{D} &= \rho \\ \nabla \cdot \mathbf{B} &= 0 \\ \nabla \times \mathbf{E} &= -\frac{\partial \mathbf{B}}{\partial t} \\ \nabla \times \mathbf{H} &= \mathbf{J} + \frac{\partial \mathbf{D}}{\partial t}, \end{aligned} \tag{2.1}$$

where $\mathbf{D}$ and $\mathbf{B}$ are the electric displacement field and the magnetic field respectively, and $\mathbf{E}$ and $\mathbf{H}$ are the electric field and the magnetising field, respectively [1;3;10]. In a nonconducting material, however, the electric current density $\mathbf{J}$ and the charge density $\rho$ are zero [10], resulting in

$$\begin{aligned} \nabla \cdot \mathbf{D} &= 0 \\ \nabla \cdot \mathbf{B} &= 0 \\ \nabla \times \mathbf{E} &= -\frac{\partial \mathbf{B}}{\partial t} \\ \nabla \times \mathbf{H} &= \frac{\partial \mathbf{D}}{\partial t}, \end{aligned} \tag{2.2}$$

Assuming time harmonic solutions, $\mathrm{e}^{-i\omega t}$ ($\omega$ being the angular frequency) and the relations

$$\begin{aligned} \mathbf{D} &= \varepsilon \mathbf{E} \\ \mathbf{B} &= \mu \mathbf{H}. \end{aligned} \tag{2.3}$$

where $\varepsilon$ and $\mu$ are material properties with an $\omega$-dependence, 2.2 reduces to

$$\nabla \times \mathbf{E} - i\omega \mathbf{B} = 0 \tag{2.4a}$$

$$\nabla \times \mathbf{B} + i\omega\mu\varepsilon \mathbf{E} = 0 \tag{2.4b}$$

$$(\nabla^2 + \mu\varepsilon\omega^2)\mathbf{E} = 0 \tag{2.4c}$$

$$(\nabla^2 + \mu\varepsilon\omega^2)\mathbf{B} = 0. \tag{2.4d}$$

$\varepsilon$ and $\mu$ are called permittivity and permeability and affects the propagation of electric- and magnetic fields, respectively[3]. They are related to their values in a vacuum (denoted $\varepsilon_0$ and $\mu_0$) through their relative permittivity, $\varepsilon_r$, and relative permeability, $\mu_r$, as $\varepsilon = \varepsilon_0\varepsilon_r$ and $\mu = \mu_0\mu_r$. In 2.4, the approximation that $\varepsilon$ and $\mu$ are real and positive is made. That means there are no losses[10]. If one consider a plane wave travelling in the x-direction, $e^{ikx-i\omega t}$, 2.4c implies that the wave number

$$k = \omega\sqrt{\mu\varepsilon}\,. \tag{2.5}$$

And the phase velocity of the wave is

$$v = \frac{\omega}{k} = \frac{1}{\sqrt{\mu\varepsilon}} = \frac{c}{n}, \tag{2.6}$$

where $c$ is the speed of light and the refractive index, $n$, is defined as

$$n = \sqrt{\frac{\mu}{\mu_0}\frac{\varepsilon}{\varepsilon_0}}\,. \tag{2.7}$$

This brief explanation of Maxwell's equations and how the electric and magnetic field interacts, enable us to understand the next sections.

## 2.2 Optical waveguide modes in planar waveguides

This section deals with the properties of the allowed modes in optical integrated systems. Optical waveguides are ubiquitous in everyday life. They are for example essential in communication systems and in computers. Planar waveguides can support waves with distinct mode characteristics. These modes can be understand as optical energy spatially distributed in one or more dimensions and remains constant in time.[9]. There are various ways of describing the behavior of light in optical systems like waveguides[1], and in this thesis the waveguide modes will be described first through a physical-optic approach and then by a ray-optic approach.

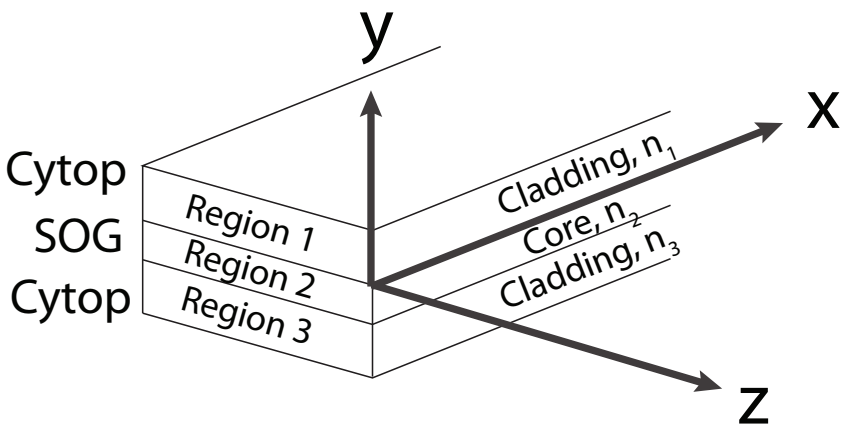


Figure 2.1: *How the waveguide is built-up. It is fabricated as two cladding layers of cytop sandwiching a core layer of SOG. The refractive indices of the cytop layers are $n_1 = n_3$ =1.34, to mimic an aqueous environment. The refractive index of SOG is $n_2$ =1.42*

### 2.2.1 Physical-optic approach

Alongside the description above, a mode can also be defined as an electromagnetic field being a solution to Maxwell's wave equation

$$\nabla^2\mathbf{E}(\mathbf{r},t) = [n^2(\mathbf{r})/c^2]\partial^2\mathbf{E}(\mathbf{r},t)/\partial t^2, \tag{2.8}$$

where $\mathbf{r}$ is the radial component vector and t is the time[1;9]. With the polar coordinate system and the relation 2.6, equation 2.4 will be written[9]

$$\nabla^2\mathbf{E}(\mathbf{r}) + k_0^2 n^2(\mathbf{r})\mathbf{E}(\mathbf{r}) = 0\,. \tag{2.9}$$

Assuming a plane wave propagating in the x-direction with propagation constant $\beta$, $\mathbf{E}(\mathbf{r}) = \mathbf{E}(y,z)\mathrm{e}^{-i\beta x}$, and an asymmetric waveguide (i.e. where $n_1 \neq n_3$ and $n_1, n_3 < n_2$, see figure 2.1) equation 2.9 is written in the three regions as

$$Region1 \qquad \partial^2 E(y,z)/\partial y^2 + (k_0^2 n_1^2 - \beta^2)E(y,z) = 0 \tag{2.10a}$$

$$Region2 \qquad \partial^2 E(y,z)/\partial y^2 + (k_0^2 n_2^2 - \beta^2)E(y,z) = 0 \tag{2.10b}$$

$$Region3 \qquad \partial^2 E(y,z)/\partial y^2 + (k_0^2 n_3^2 - \beta^2)E(y,z) = 0, \tag{2.10c}$$

where $E(y,z)$ is the electrical field component of $\mathbf{E}(y,z)$ in the respective region.

The solutions of equation 2.10 in these three regions are either sinusoidal or exponential functions, depending on whether the term $(k_0^2 n^2 - \beta^2)$ is positive or negative in that region. And of course both $E(y,z)$ and $\partial E(y,z)/\partial y$ have to be continuous over the region boundaries[9].

The different mode shapes that can be supported by the waveguide are visualised in figure 2.2. Mode A, when $\beta < k_0 n_1$, is referred to as air radiation mode while mode B, where $k_0 n_1 < \beta < k_0 n_3$, is called substrate radiation mode and mode C and D, where $k_0 n_3 < \beta < k_0 n_2$, are the the fully confined propagation modes[2].

For an air radiation mode, the solution is an exponential function in all three regions (see mode A of figure 2.2). For the substrate radiation mode, the solution in region 1 is exponentially attenuating while it in region 2 and 3 still are exponential solution functions (see mode B of figure 2.2).

For fully confined propagation modes, the solution is sinusoidal in region 2 but exponentially attenuating in both region 1 and 3, see modes C and D in figure 2.2. This is the kind of mode being used in the latter stages of this thesis. Mode C of figure 2.2 is the fundamental transverse electric mode, TE0, and mode D is the first higher order mode, TE1. If, mathematically, $\beta$ would be larger than $k_0 n_2$, the solution would end up as mode E in figure 2.2, where the solution functions would be exponentially increasing towards infinity. But this mode is not physically feasible due to the exponentially growing electric fields in region 1 and 3, implying infinite energy, and can therefore be discarded.

The air radiation mode and the substrate radiation mode are not well suited for signal transmission. As the wave propagates, region 2 will continually lose energy (the substrate radiation mode to it's oscillatory part in region 3, and the air radiation mode to both region 1 and 3) and they will therefore be damped out over a short distance[9].

### 2.2.2 Ray-optic approach

The previous section followed the physical-optic approach to describe how and which light modes can be supported by a waveguide. Another way to describe the same phenomenon is through the ray-optic approach. The light in the physical-optic approach was represented by an electromagnetic field which is a solution to Maxwell's wave equation, leading to plane waves propagating in the x-direction.

In the ray-optic approach, the light is described by light-rays experience total internal reflection in a zig-zag path within the waveguide. The rays represent the normals of plane waves propagating in the waveguide as shown in figure 2.4.

Starting with equation 2.10, the electric field $E_z$ in region 2 of figure 2.2 will according to the ray-optic description have the form

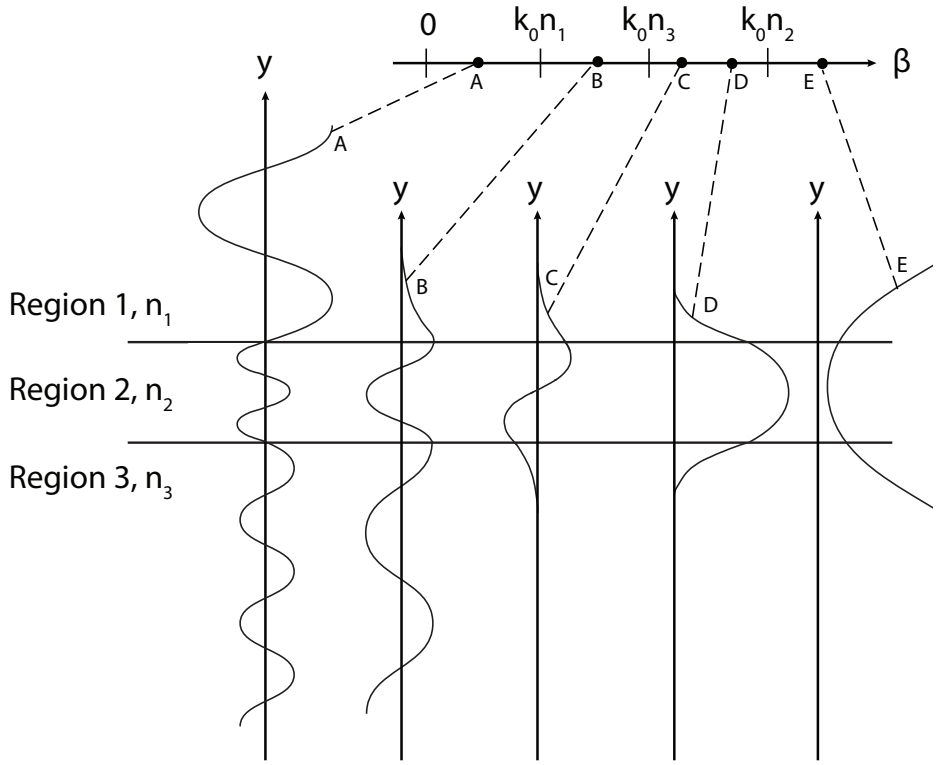


Figure 2.2: *Possible modes for the electrical field as a function of propagation constant $\beta$. $\beta$ can be specific discrete values according to which mode it corresponds to. Intern relation between the refractive indices is $n_1 < n_3 < n_2$. Mode A is an air radiation mode, mode B is a substrate radiation mode. Mode C and D are fully confined modes supported by the waveguide. Mode D is the mode gained in the waveguide used in this thesis. Mode E is only mathematically, but not physically, attainable.*

$$E_z(x,y) \propto sin(hx + \gamma), \tag{2.11}$$

where $h$ and $\gamma$ varies with the properties of the particular waveguide.[9] Notice that $E_z$ now is a function of both $x$ and $y$ in contrast to the physical-optic approach where the solution only depends on $x$. Combining equation 2.10 and 2.11 will render in the condition

$$\beta^2 + h^2 = k_0^2 n_2^2. \tag{2.12}$$

Here it is noticeable that both $\beta$, $h$ and $k_0 n_2$ are propagation constants with dimension $1/m$; $\beta$ in x-direction, $h$ in the y-direction and $k_0 n_2$ along the light ray, compare in figure 2.4. Since the frequency $\omega$ is constant, the plane waves which each mode comprise will travel with the same phase velocity while $\beta_m$ and $h$ are parameters associated with the $m$th mode[9]. Every allowed waveguide mode, $m$, has a corresponding propagation constant $\beta$ given by[9;16]

$$\beta_m = k_0 n_2 sin(\phi_m) = k_0 n_2 cos(\theta_m). \tag{2.13}$$

$\beta_m$, $h$ and $k_0 n_2$ relate to each other as can be seen in figure 2.3 and with $\theta_m$ beeing the angle with which the wave is travelling relative to the x-axis. $\phi$ is the angle between $h$ and $k_0 n_2$.

The light mode where $m = 0$ is usually referred to as the fundamental mode while other modes having $m \geq 1$ are called higher-order modes[16].

Recall figure 2.3 and Snell's law[15]

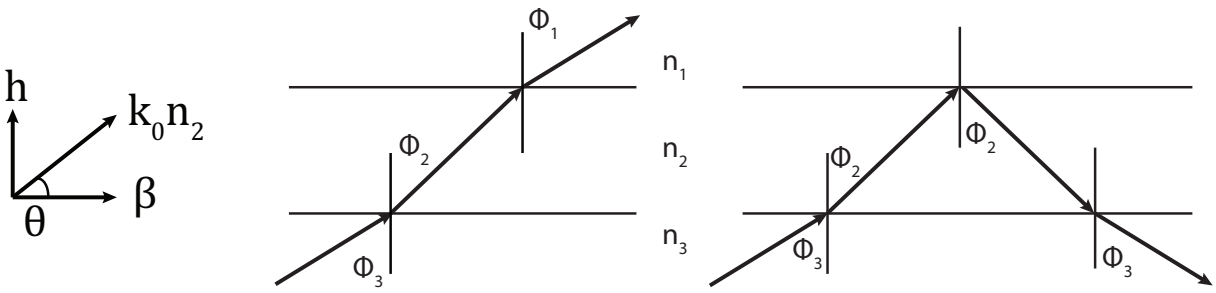


Figure 2.3: *Denotation of the angles given an account of. Ray paths of air radiation mode (left) and substrate radiation mode (right). The incident angle and the refractive indices decide whether it is going to be an air radiation mode, a substrate radiation mode or a fully confined mode, in which case the light would be totally internally reflected both in the interface between substrate 1 and 2 and between substrate 2 and 3.*

$$n_1 sin(\phi_1) = n_2 sin(\phi_2) \tag{2.14}$$

to define the condition of total reflection between the boundaries of region 1 and 2 and between region 2 and 3 [16]

$$\phi_2 \geq sin^{-1}(n_1/n_2) \tag{2.15a}$$

and

$$\phi_2 \geq sin^{-1}(n_3/n_2), \tag{2.15b}$$

respectively.

These equations relates to figure 2.3. To the left in the figure is an air radiation mode shown, where $\phi_3$ not is large enough for total reflection in neither the boundary between medium 1 and 2 nor between 2 and 3. To the right in figure 2.3 is a substrate radiation mode shown, where $\phi_3$ is large enough for the ray to be totally reflected in the 1-2-boundary but not large enough to confine it in the waveguide core. This relates to equation 2.15a. If $\phi_3$ would be large enough to satisfy the condition of 2.15b, the light ray would be confined to region 2.

To resume the comparison with the physical-optic approach, $\phi_2$ can be taken from figure 2.3 as $sin(\phi_2) = \beta/k_0 n_2$. Thus, as discussed around equations 2.10 if $\beta \leq k_0 n_1$, it will lead to

$$sin(\phi_2) = \beta/k_0 n_2 \leq k_0 n_1/k_0 n_2 = n_1/n_2 \tag{2.16}$$

which relates to an air radiation mode and corresponds to mode A in figure 2.2 and the left ray path in figure 2.3. Equivalent, $k_0 n_1 \leq \beta \leq k_0 n_3$ relates to a substrate radiation mode

$$n_1/n_2 \leq sin(\phi_2) \leq n_3/n_2 \tag{2.17}$$

as can be seen in figures 2.2 and 2.3 and only if $k_0 n_3 \leq \beta \leq k_0 n_2$ it will correspond to confined waveguide modes

$$sin(\phi_2) = \beta/k_0 n_2 \geq k_0 n_3/k_0 n_2 = n_3/n_2. \tag{2.18}$$

Notice that equations 2.16 − 2.18, derived from the physical-optic approach, agree with the corresponding equations of 2.15 derived with the ray-optic approach. [9]

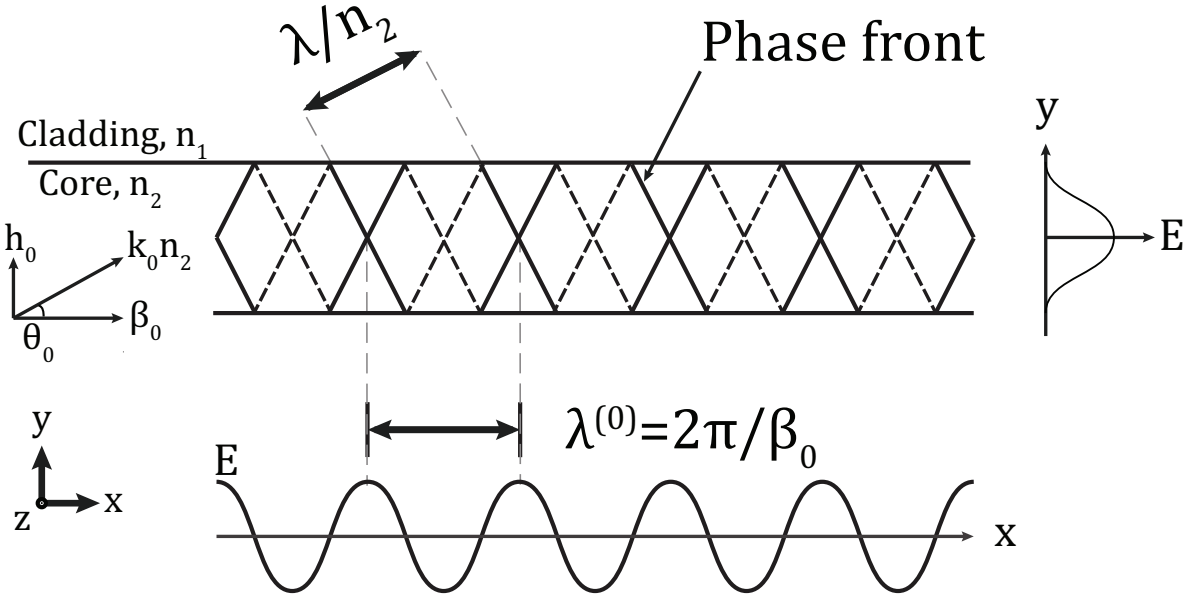


(a) *Fundamental mode, TE0.*

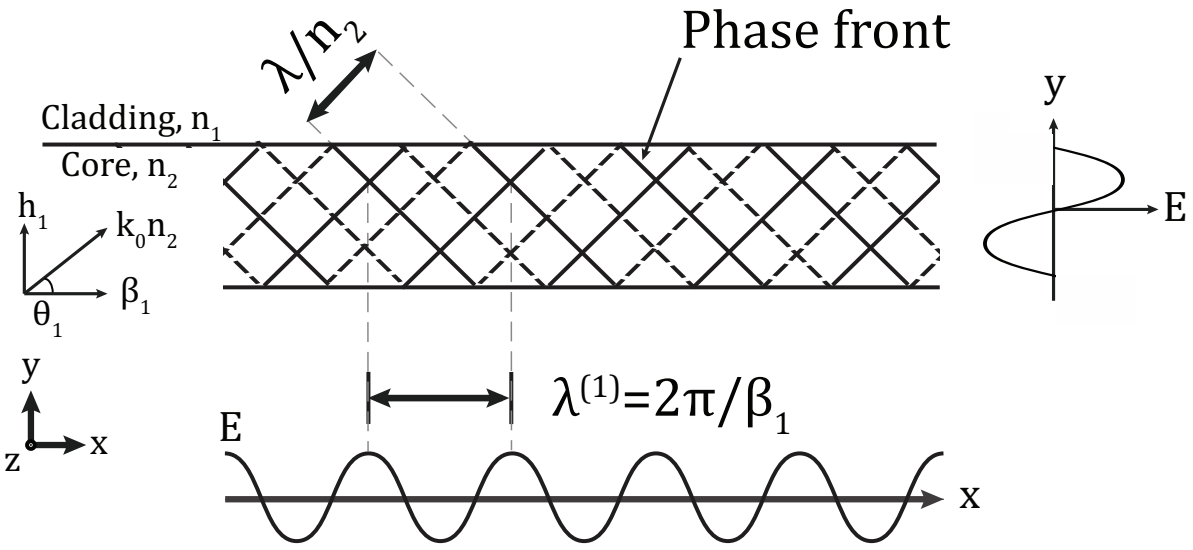


(b) *First order of higher order modes, TE1.*

Figure 2.4: *Formation of modes (standing waves) by the ray-optic approach. The solid lines represent positive phase front and the dashed lines represent negative phase fronts. Whenever two positive (negative) phase fronts intersect, there is a maximum (minimum) in the electric field. In this way, standing waves appear periodically along the x-direction with the period lambda* $= 2\pi/\beta$ [16]*. Denotations as above.*

## 2.3 The three-layer planar waveguide

Consider the three-layer planar waveguide of figure 2.1. Maxwell's equation reduces to (compare with equation 2.8):

$$\nabla^2 E_z = \frac{n^2}{c^2}\frac{\partial^2 E_z}{\partial t^2}, \tag{2.19}$$

with solutions in the three regions on the form

$$E_z(x,y,t) = \mathcal{E}_z(y)\mathrm{e}^{i(\omega t-\beta x)} \ . \tag{2.20}$$

As described in section 2.2.1, the general form of $\mathcal{E}$ will be

$$\mathcal{E}_z(y) = \begin{cases} A\mathrm{e}^{-qy} & 0 < y < \infty \\ B\cos hy + C\sin hy & -t_g \leq y \leq 0 \\ D\mathrm{e}^{[p(y+t_g)]} & \infty < y < -t_g \, . \end{cases} \tag{2.21}$$

For transverse electric waves, TE, polarised in the z-direction, the x- and y-components are zero. Note that the solution has no dependence in x or z due to the approximation that the slabs are assumed to be infinite in those directions. Taking into account the boundary conditions that $E_z$ and $\partial E_z/\partial y$ have to be continuous at the boundaries $y = 0$ and $y = -t_g$, this will lead to an equation with only a single unknown parameter $A$:

$$E_z = \begin{cases} A\mathrm{e}^{-qy} & 0 < y < \infty \\ A[\cos hy - (q/h)\sin hy] & -t_g \leq y \leq 0 \\ A[\cos ht_g + (q/h)\sin ht_g]\mathrm{e}^{p(y+t_g)} & -\infty < y < -t_g \ . \end{cases} \tag{2.22}$$

$A$ is an arbitrary constant and $q$, $h$ and $p$ can be determined by substituting 2.22 into 2.20:

$$\begin{aligned} q &= (\beta^2 - n_1^2 k_0^2)^{1/2} \\ h &= (n_2^2 k_0^2 - \beta^2)^{1/2} \\ p &= (\beta^2 - n_3^2 k_0^2)^{1/2} \ . \end{aligned} \tag{2.23}$$

Notice that for fixed refractive indices, $q$, $h$ and $p$ are only dependening on one parameter, $\beta$. Only three out of four boundary conditions are used, so by making $\partial E_z/\partial d_y$ continuous at $x = -t_g$, also a fourth condition can be generated:

$$tan(ht_g) = \frac{p+q}{h(1-pq/h^2)} \ . \tag{2.24}$$

From this equation the propagation constant $\beta$ can be determined. $\beta$ will take one discrete value per allowed mode, that is when it fulfills the condition $k_0 n_3 < \beta < k_0 n_2$.[9]

### 2.3.1 Cutoff condition

If for example the bottom layer of the planar waveguide is made out of a material with slightly lesser refractive index than the transmitting layer in region 2, and where the the top layer is left open to the air, i.e. $n_1 \neq n_3$. These waveguides are called asymmetric and will form asymmetric wave modes. In this report the waveguide studied is symmetric (i.e. $n_1 = n_3$), which ease the calculations when determining which modes may be supported.

For a symmetric waveguide, the lower boundary for $\beta$ is when the electric fields in regions 1 and 3 becomes oscillatory, i.e.[9]

$$\beta = k_0 n_1 = k_0 n_3 \, . \tag{2.25}$$

Substituting equation 2.25 into 2.23 yields

$$p = q = 0 \tag{2.26a}$$

and

$$h = k_0\sqrt{n_2^2 - n_1^2} = k_0\sqrt{n_2^2 - n_3^2}\,. \tag{2.26b}$$

Substituting 2.26a into 2.24 yields

$$tan(ht_g) = 0 \tag{2.27a}$$

and

$$ht_g = m\pi \quad ;m = 0,1,2,...\,, \tag{2.27b}$$

which together with equation 2.26b result in

$$k_0\sqrt{n_2^2 - n_1^2}t_g = m\pi. \tag{2.28}$$

By dividing equation 2.28 by $k_0 t_g$, taking the square of it and divide by $(n_2 - n_1)$, the result gained is the so called cutoff condition for the symmetric waveguide:

$$\Delta n = (n_2 - n_1) > \frac{m^2\lambda_0^2}{4t_g^2(n_2 - n_1)} \quad ;m = 0,1,2,...\,. \tag{2.29}$$

That means that for given waveguide parameters, such as thickness and refractive index, the number of bound modes can be determined, and vice versa, for a given mode $m$, the parameters $n_1$, $n_2$, $n_3$, $t_g$ and $\phi_m$ (or $\theta_m$) can be calculated.[9] Note that there is no cutoff limit for the fundamental mode as $m = 0$.

## 2.4 Scattering theory

The purpose of the following section is to give a brief description of the scattering theory applied in the thesis. Scattering of electromagnetic waves originates from the inhomogeneity of the medium in which the waves are travelling. Every inhomogeneity, regardless whether it is a single electron, a molecule or a larger particle, is a source for scattering[5]. When the electrons of a metallic particle interacts with an external electric field, the particle's electron cloud will be displaced. There will be a restoring force due to Coulomb attraction between the electrons and the nuclei and the electrons will begin to oscillate with the plasma frequency. The plasma frequency depends on the electron density and the electron mass and is sometimes denoted dipole particle plasmon resonance. The resonance can be calculated as

$$m^2 = \frac{\varepsilon_{metal}}{\varepsilon_{solution}} = -2\,, \tag{2.30}$$

where $m$ is the relative refractive index, $m = n_{metal}/n_{solution}$, and $\varepsilon_{metal}$ and $\varepsilon_{solution}$ are the dielectric functions of the particle and the surrounding medium, respectively.[4;19] Consequently, the plasma frequency for gold nanoparticles in water lies around 520 - 550 nm[11;12;18;19]. The range is a consequence of the fact that larger particles cannot be viewed as point dipoles, causing a retarding red-shift and a decreasing plasma frequency for larger particles[19].

As the charges in the scattering particle oscillate, they will also radiate. This secondary radiation is called scattering. The real part of gold's refractive index is largely negative in comparison to an aqueous surrounding, yielding the scattering[19]. If the particle converts some of the incident radiation into other forms of energy, e.g. thermal energy, the total energy leaving the particle is less than the energy flow towards the particle[10]. This process is called absorption[5;10]. The scattering is elastic, while the absorption is inelastic[12]. Together the scattering and absorption make up the extinction, that is the attenuation of a beam of light travelling in a sample of multiple scatterers[5;8;12;19]. Scattering is a good method for detecting nanoparticles. Gold nanoparticles sized 80 nm show light emissions five orders of magnitude stronger than strong fluorescing dyes[11].

### 2.4.1 Radial dependence of the scattering

When calculating extinction, absorption and scattering, it is normal to use the cross-section. Cross-section is measured in $m^2$ because it represents an equivalent cross-sectional area that interact, and contribute to, the extinction, absorption and scattering [11]. The scattering cross-section is calculated by integrating the scattered power in all directions of the far-field of the sphere and divide it by the intensity. Similar, the absorption cross-section is calculated as the net energy inflow divided by the intensity. [19] The scattering cross-section for particles that are much smaller than the wavelength varies with the radius of the sphere, $R$, as $R^6$, while the absorption cross-section goes as $R^3$ [4;18;19]. Therefore, absorption is more important than scattering for small particles ( $\leq 150$ nm), while scattering becomes more important when the circumference of the spheres can be compared to the wavelength [4;11;12;18;19].

### 2.4.2 Rayleigh scattering

Consider an arbitrary shaped particles being illuminated by a plane wave which propagation is in the x-direction,

$$u_0 = \mathrm{e}^{i(\omega t - kx)}\,, \tag{2.31}$$

with the same symbol conventions as earlier. The particle will scatter the light wave, which in the far distance will form a spherical outgoing wave which amplitude is inversely proportional to the distance, $r$, from the particle [8]. Thus, it can be written

$$u = \mathcal{S}(\theta)\frac{\mathrm{e}^{i(\omega t - kr)}}{ikr}\,, \tag{2.32}$$

where $\theta$ is the angle that the scattered wave makes with the incoming wave. Combining the two equations gives

$$u = \mathcal{S}(\theta)\frac{\mathrm{e}^{ik(x-r)}}{ikr}u_0\,, \tag{2.33}$$

where $\mathcal{S}$ is defined as the amplitude function and has a $\theta$ dependence. The amplitude function can also be written as

$$\mathcal{S}(\theta) = s \cdot \mathrm{e}^{i\phi} \tag{2.34}$$

where $s$ and $\phi$ are functions of $\theta$ and $s$ is the positive amplitude and the phase $\phi$ is real. Let $I_0$ be the intensity of the incoming wave and $I_{sca}$ the intensity of the scattered wave. As the intensity is proportional to the square of the amplitude, it follows that

$$I_{sca} = \frac{s^2(\theta)}{k^2 r^2} I_0\,. \tag{2.35}$$

The polarisation of the wave should also be taken into account, the scattering in any arbitrary direction is given by a set of amplitude functions $\mathcal{S}_1$, $\mathcal{S}_2$, $\mathcal{S}_3$ and $\mathcal{S}_4$. Hence, the incident and scattered electric fields will be connected to each other as

$$\begin{pmatrix} E_l \\ E_r \end{pmatrix} = \begin{pmatrix} \mathcal{S}_2 & \mathcal{S}_3 \\ \mathcal{S}_4 & \mathcal{S}_1 \end{pmatrix} \cdot \frac{\mathrm{e}^{ik(x-r)}}{ikr} \begin{pmatrix} E_{l0} \\ E_{r0} \end{pmatrix} \tag{2.36}$$

where $E_l$ and $E_r$ represent the electric field's components parallel and orthogonal to the plane of scattering, respectively. [5;8]

### Spherical particles

For scattering on spherical particles $\mathcal{S}_3 = \mathcal{S}_4 = 0$ [8], resulting in the equations

$$\begin{aligned} E_r &= \mathcal{S}_1(\theta)\frac{e^{ik(x-r)}}{ikr}E_{r0} \\ E_l &= \mathcal{S}_2(\theta)\frac{e^{ik(x-r)}}{ikr}E_{l0} \quad , \end{aligned} \tag{2.37}$$

which describes the electric field in any arbitrary direction ($\theta \neq 0$). Taking the square of equation 2.37 will give the intensities for perpendicular

$$I = \frac{|\mathcal{S}_1|^2}{k^2r^2}I_0 \tag{2.38a}$$

and parallel polarisation

$$I = \frac{|\mathcal{S}_2|^2}{k^2r^2}I_0 \ . \tag{2.38b}$$

As a particle is excited by the incident electromagnetic field it starts to oscillate with the field and becomes a dipole. The oscillating dipole radiates in all directions. This is called Rayleigh scattering. Let $\mathbf{E_0}$ be the homogeneous electric field in which the particle is situated, and let $\mathbf{p}$ be the induced dipole of the particle. The particle's scattering radiation will interact with the background field so let the combined field be denoted $\mathbf{E}$. Then $\mathbf{p} = \boldsymbol{\alpha}\mathbf{E_0}$, where $\boldsymbol{\alpha}$ is the polarisability of the particle. If the polarisability is isotropic, which is the common case [8], it can be treated as a scalar leading to $\mathbf{p}$ and $\mathbf{E_0}$ always coinciding. Henceforth the electric field of the scattered wave is [8]

$$E = \frac{k^2 psin(\theta)}{r}e^{-ikr}. \tag{2.39}$$

The corresponding intensity of the scattered radiation is then

$$I = \frac{c}{8\pi}|E|^2 \tag{2.40}$$

and by integrating the intensity over a large sphere the total scattered energy per unit time is

$$W = \frac{1}{3}k^4 c|p|^2 \, . \tag{2.41}$$

The scattering cross section is a theoretical measure of the likelihood of the particle to scatter the light and is derived [8;10] by dividing 2.41 by $I_0$ as

$$\sigma_{sca} = \frac{8}{3}\pi k^4 |\alpha|^2 \, . \tag{2.42}$$

With this knowledge, it can be shown [8] that the scattering tensor is

$$\begin{pmatrix} \mathcal{S}_2 & \mathcal{S}_3 \\ \mathcal{S}_4 & \mathcal{S}_1 \end{pmatrix} = ik^3\alpha \begin{pmatrix} cos(\theta) & 0 \\ 0 & 1 \end{pmatrix} \tag{2.43}$$

and that the scattered intensity is

$$I = \frac{(1 + cos^2(\theta)k^4 |\alpha|^2)}{2r^2}I_0. \tag{2.44}$$

Thus, since $k = 2\pi/\lambda$, the scattering intensity is dependent on the wavelength as $I \propto 1/\lambda^4$ [6;10]. A visualisation of 2.44 is made in figure 2.5. The figure shows how a spherical particle that is small compared to the wavelength scatters light. This approximation is called the Rayleigh approximation [7].

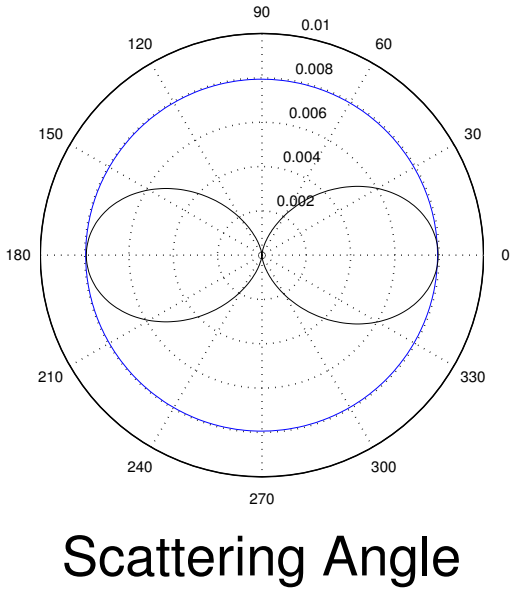


Figure 2.5: *A figure of how a spherical particle, small in comparison to the wavelength, scatter an incident plane electromagnetic wave. The outer circle indicates that the polarisation is perpendicular to the plane of drawing and the peanut shaped line represents the polarisation parallel to the plane of drawing. The scale is arbitrary.*

### 2.4.3 Mie theory

Mie theory is the theory that examines how a spherical particle scatters electromagnetic radiation. Mie presupposed a homogeneous sphere under illumination of plane electromagnetic waves.[7] As seen above, scattering depends on the wavelength of the light. But it also depend on the particle size $a$.[5;6;10] One convenient way of combining these parameters is to define a new reduced size parameter $q = 2\pi a/\lambda$. Figure 2.5 visualise scattering of a sphere where $q$ is small ($q \ll 1$). Mie and Debye were the first ones to analyse scattering when $q$ no longer is small, reasoning that it is a complicated problem[10]. Wolf[6] and Bohren[5] have tried to show the dependence of the scattering behaviour of $q$, as shown in figure 2.6.

As $q$ exceeds unity, i.e. when the diameter of the sphere is greater than $\lambda/\pi$, there will appear more and more maxima- and minima lobes in the polar scattering plots[6]. Bohren & Huffman[5] and van de Hulst[8] have used the Mie theory to work out a method to numerically determine the appearance of the scattering lobes. Mie's theory for spherical particles of radius $R$ gives a series expansion of the extinction and scattering cross-sections that includes Bessel functions of the parameter $q$ and $m$ (both as above)[19]. Without further explanation here, the two key parameters for the Mie calculations are the scattering parameters $a_n$ and $b_n$[11;13]

$$\begin{aligned} a_n &= \frac{m^2 j_n(mq)[qj_n(q)]' - \mu_1 j_n(q)[mqj_n(mq)]'}{m^2 j_n(mq)\left[qh_n^{(1)}(q)\right]' - \mu_1 h_n^{(1)}(q)[mqj_n(mq)]'} \\ b_n &= \frac{\mu_1 j_n(mq)[qj_n(q)]' - j_n(q)[mqj_n(mq)]'}{\mu_1 j_n(mq)\left[qh_n^{(1)}(q)\right]' - h_n^{(1)}(q)[mqj_n(mq)]'}, \end{aligned} \tag{2.45}$$

where $m$, as above, is the the refractive index relative to the ambient medium and $\mu_1$ is the ratio of the permeability of the sphere to the permeability of the surrounding medium. $j_n$ and $h_n^{(1)}$ are spherical Bessel function and spherical Hankel function of order $n$, respectively. Together with the recurrence functions[5;7;11;13]

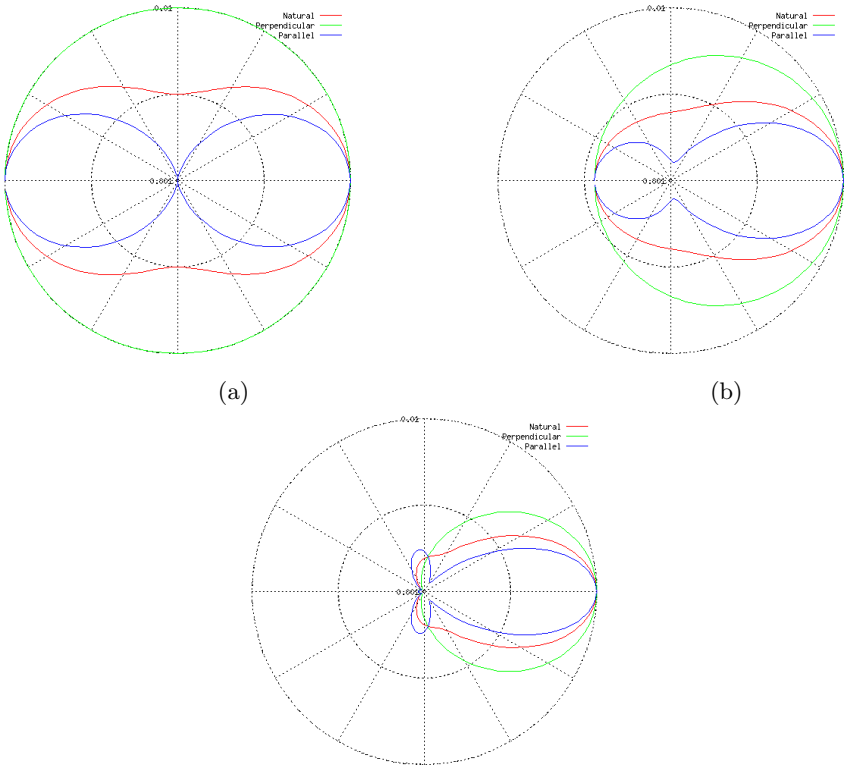


Figure 2.6: *Polar diagrams of the q-dependence of the scattering. q is increasing from being* $\ll 1$ *in (a) to almost 1000 in (c). The tendency is more forward scatter, the greater q becomes.*

$$\begin{aligned} \pi_n &= \tfrac{2n-1}{n-1} cos(\theta)\pi_{n-1} - \tfrac{n}{n-1}\pi_{n-2} \\ \tau_n &= ncos(\theta)\pi_n - n + 1\pi_{n-1}, \end{aligned} \tag{2.46}$$

beginning with $\pi_0 = 0$ and $\pi_1 = 1$, the scattering amplitudes can be calculated as

$$\mathcal{S}_1(cos\theta) = \sum_n \frac{2n+1}{n(n+1)}(a_n\pi_n + b_n\tau_n) \tag{2.47a}$$

and

$$\mathcal{S}_2(cos\theta) = \sum_n \frac{2n+1}{n(n+1)}(a_n\tau_n + b_n\pi_n)\,. \tag{2.47b}$$

With these formulae and a calculation program, it is possible to calculate the polar scattering diagrams of e.g. figure 2.6.

# 3
# Methodologies and materials

The work with this thesis was planned and carried out in two parts. The first part was more oriented towards theory and simulation, while the second part was purely experimental. For the simulations COMSOL Multiphysics version 4.3a was used, and the experimental part was carried out in the Bio-lab at Chalmers University of Technology in the division of biological physics.

## 3.1 Simulations

As a multi modelling program, Comsol can combine different areas of physic which makes it a powerful tool for numerical computation. In this thesis the version Comsol 4.3a was used, primarily to emulate the waveguide theory (see section 2.3) and the scattering theory (see section 2.4.3). The original plan was thereafter to also use it as an optimisation tool for some experimental parameters such as particle size and laser wavelength. Unfortunately time ran short and the simulations had to end ahead of the optimisation process.

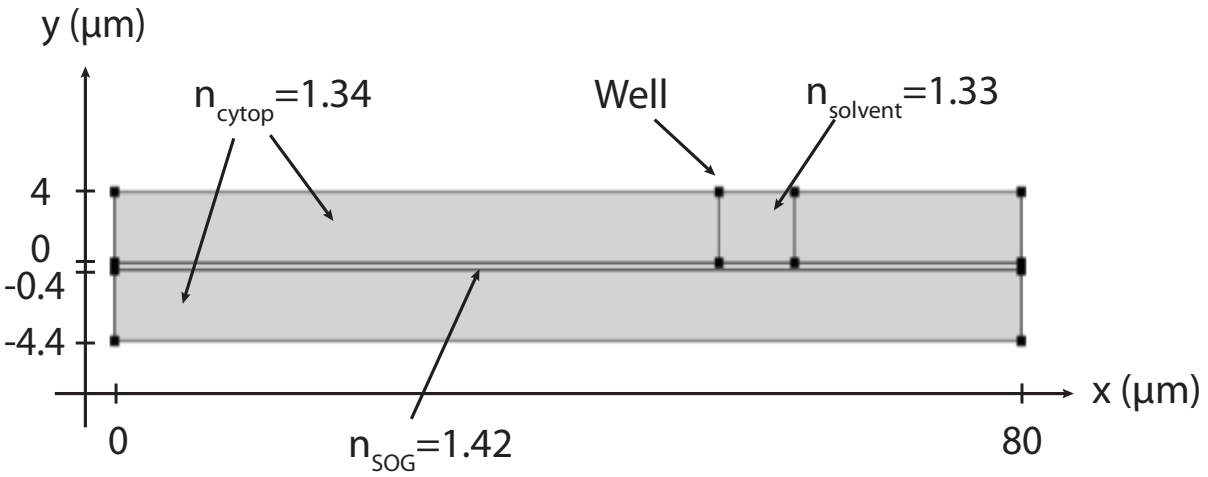


Figure 3.1: *The figure is a two-dimensional representation of the waveguide. The electromagnetic field is introduced at the left boundary of the channel, i.e. the middle layer. Also, the two vertical lines on top of the channel mark where the well is situated.*

### 3.1.1 Two-dimensional model

The first step of the simulations in Comsol was to build a two-dimensional model to simulate how the entering electromagnetic field would distribute inside the waveguide. That simulation was then compared to the theory described in section 2.3. The geometry of the two-dimensional model can be viewed in figure 3.1. The top- and bottom cytop layers have an index of refraction set to $n_{cytop} = 1.34$ while the core layer was set to $n_{SOG} = 1.42$ and the material in the well was $n_{solvent} = 1.33$.

### 3.1.2 Three-dimensional model

The second step of the simulations was to create a three-dimensional model to simulate how a gold particle of nano size would scatter an incoming field. This was successful in the sense that it agreed with the theory, as far as a plane wave was used as incoming light source. The model can be seen in figure 3.2. The diameter of the gold particle was 30 nm while the solution layer and the PML (Perfectly Matched Layer) had a thickness of $\lambda/2$. The PML is placed half a wavelength away for not being within the reacting near-field region of the scatterer. The simulation geometry only contains a quarter of a sphere. This is enough due to symmetry in the electric and magnetic fields. It is implemented through correctly set boundary conditions. The module used in Comsol was the radio frequency module for electromagnetic waves in the frequency domain. A deeper look into the exact procedure is given in appendix A.

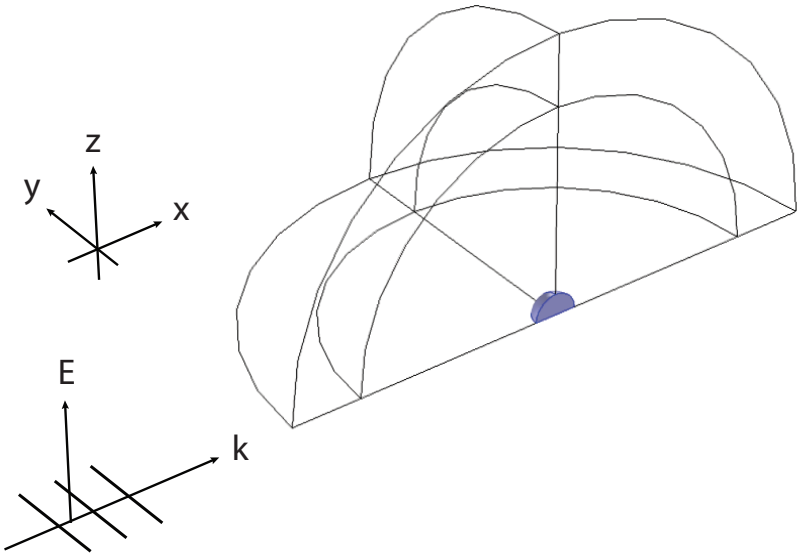


Figure 3.2: *As the incoming electromagnetic field is magnetically symmetric along the vertical axis and electrically symmetric along the horizontal axis, with the right boundary conditions only a quarter of the gold sphere has to be modelled.*

As mentioned, unfortunately this marked the end of the simulations. Due to time constraints the planned combination of the two models was never performed. If it would have been performed, the field from the two-dimensional model would have been used as a background field in the three-dimensional model.

## 3.2 Experiments

The experimental part of this thesis was made at a bio-lab in collaboration with Mathias Elmeskog and Björn Agnarsson at Chalmers' department of Applied physics at the division of Biological physics. To study the behaviour of nanoparticles in the vicinity of an evanescent waveguide field, waveguide chips made by Agnarsson were used. For a picture of how the waveguide looks like and the concept behind the scattering, see figure 3.3.

### 3.2.1 The waveguide chip

The waveguide chip is a three-layer planar waveguide as described in section 2.3. It is sketched in figure 2.1. The dimensions of the chip are 1×1 cm and the well measures 2×2 mm. The depth of the well is 4 $\mu$m. The waveguides used were constructed of three wafers as pictured in figure 2.1.

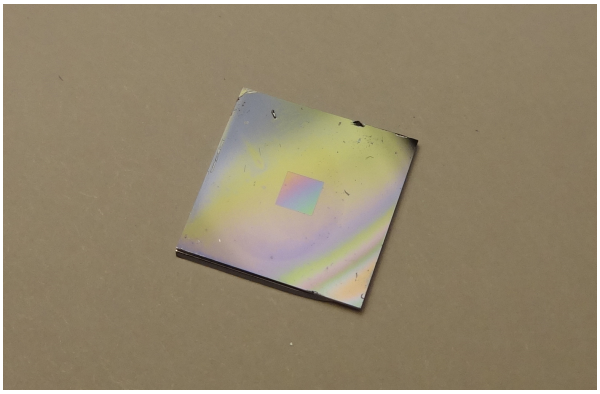

(a) *A picture of how the waveguide chip looks like. The well can be seen in the middle of the chip. In the middle of the chip, the top cytop layer is etched away to create the well. This is a discarded chip, as can be seen from its scratches.*

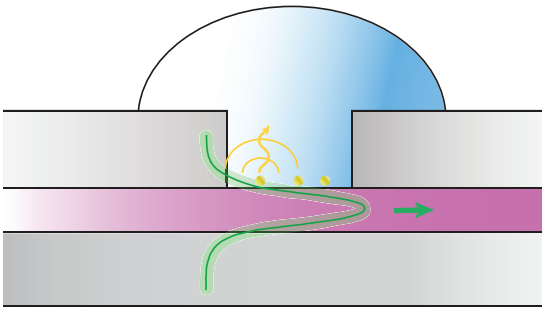

(b) *A figure of the concept behind the waveguide. It shows the waveguide well and the supported light mode. The gold particles will land on the bottom of the well and will scatter the evanescent part of the light mode. The proportions of the figure are not to scale.*

Figure 3.3: *Figure (a) is a picture of the waveguide chip and figure (b) shows the idea behind how to detect the gold nanoparticles.*

The two outer layers of the waveguide consist of cytop which is a fluorinated polymer. The middle layer is the core layer and consists of spin on glass (SOG). Since the bottom and the top layers are made of the same material, the waveguide is symmetric. SOG has higher refractive index than cytop, which means that it will support a confined mode within the core.

In order to be able to study the nanoparticles, the gold nanoparticles − and only the gold nanoparticles − have to attach to the core layer surface inside the well. This requires a bit of preparation. First of all, the chip has to be cleaned to remove all organic contaminations from e.g. the fabrication process or from careless handling. It is done in a plasma cleaner for fifteen minutes. After that, the chip surface has to be silanised in order for the gold nanoparticles to attach to it. The chip has to be handled carefully with a pair of tweezers and transported in a beaker of deionised water (hereafter called just water), to avoid unwanted dust particles attaching onto the surface.

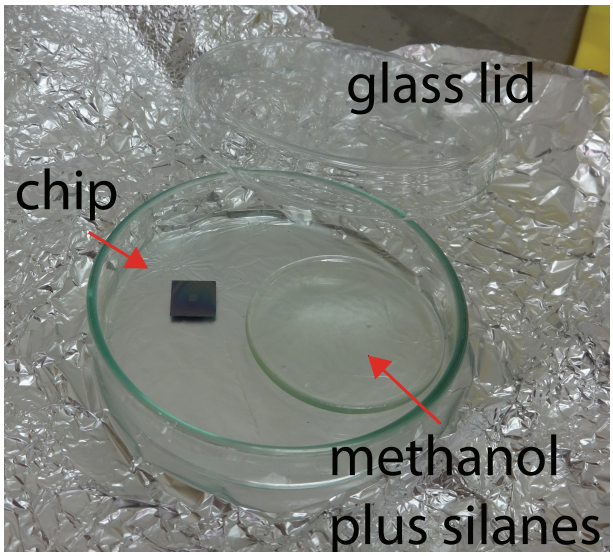


Figure 3.4: *Figure of the arrangement of the silanisation device. The chip is put in the bigger glass dish alongside the lens-shaped smaller dish where methanol and silane are mixed. The glass lid is put on, and the silanes are evaporated onto the chip surface.*

#### Silanisation

Both the gold particles and the glass surface are negatively charged. Thus, in order for the gold nanoparticles to attach, the surface has to be functionalised by a layer of 3-Aminopropyldimethylethoxsilane (APDMES, abcr GMbH & Co. Germany). The silanes bind covalently to the glass, resulting in a positively charged surface. When silanising the surface, 50 $\mu$l silanes were mixed with the same amount of methanol and put in a lens shaped glass dish. That dish stood in a larger glass dish with a glass cover together with the chip that was going to be silanised, see figure 3.4. The glass dish is sealed and left for the the silanes to evaporate onto the chip surface.

The dish was left for an hour for all the chip surface to be covered by silanes. After one hour, the chip was washed by dilution of methanol. That action was made to wash away possible loose silane layers to only leave a monolayer of silanes on the surface. After that it is rinsed and put in water for some time. The water will absorb an electron, making the surface positively charged. Between all steps of the process, the chip was dried in a stream of nitrogen in order not to leave any residues from the previous steps.

### 3.2.2 Fabrication of gold nanoparticles

As can be seen in section 3.3, the size of the particles studied were about 10 nm, 20 nm, 30 nm and 65 nm in diameter. The 30 nm particles were formed by Elmeskog, the 10 nm and the 65 nm large particles were made by Anders Lundgren and the 20 nm gold particles were formed by myself under supervision of Lundgren.

The 20 nm gold particles were precipitated out of gold ions, $HAuCl_4$ 10%, by reduction of two reducing agents, sodium citrate 1% and tannic acid 1%. In one beaker, the tannic acid and the weak base of sodium citrate were blended in the proportions of 16 ml water, 4 ml sodium citrate and 5 $\mu$l tannic acid. In another beaker, 100 $\mu$l of the gold ions were mixed with 80 ml of water. The two mixtures were heated to 60 °C. While stirred, they were mixed and heated to 95 °C and then left to cool. By then, the colour of the mixture had become bright red - as expected of nano sized gold particles.

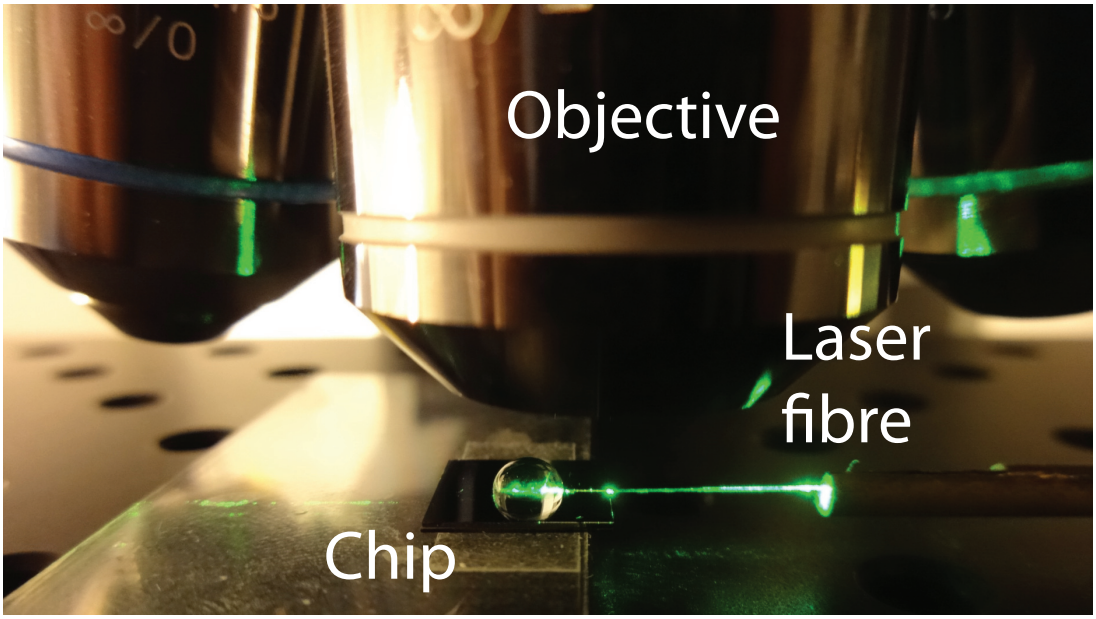


Figure 3.5: *Picture of the waveguide chip setup under the microscope. The laser fibre is aligned up against the edge of the chip in order to excite the waveguide. For measurements, the sample is inserted into the water droplet by a pipette and the object is changed to a wet 100× magnitude objective. The water droplet is placed above the well to fill it up and enable the gold nanoparticles to diffuse to the SOG surface for detection. The evanescent field will be scattered by particles on, or close to, the SOG surface, i.e. at the bottom of the well.*

### 3.2.3 Setup

When the chip had been silanised and the gold nanoparticles had been formed, the chip had to be mounted under the microscope and aligned with the green laser of wavelength 532 nm, see figure 3.5.

#### Microscope

The microscope used was an upright Olympus BX61 and the laser cable ended in a fibre that had to be aligned to the edge of the waveguide chip. The edges can vary from each other due to how the chips are broken apart, so a rough estimation of which of the edges that is the most suited has to be made. To align the laser fiber to the edge, the 2× and 20× magnification objectives were used, see figure 3.5.

After the laser had been aligned, the edge of the waveguide well had to be found. When it was found, a droplet of water or water mixed with citrate buffer was pipetted over the well. This enabled the wet 100× objective to be used.

When the edge of the well was found and focus obtained, a EMCCD camera detected the scattered field from the waveguide. For recording a sequence of pictures from the microscope, the program Micro-Manager 1.4 was used. It recorded a picture each second, creating a sequence of pictures that was saved as a .tif file.

#### Mobile phone

As for Micro-Manager, the same sequence was recorded by the mobile phone by the application O Snap. Though, to save memory, O Snap only recorded a picture every fifth second.

The mobile phone was mounted upon the ocular of the microscope, so the pictures recorded were just what also could be seen by the eye, see figure 3.6.

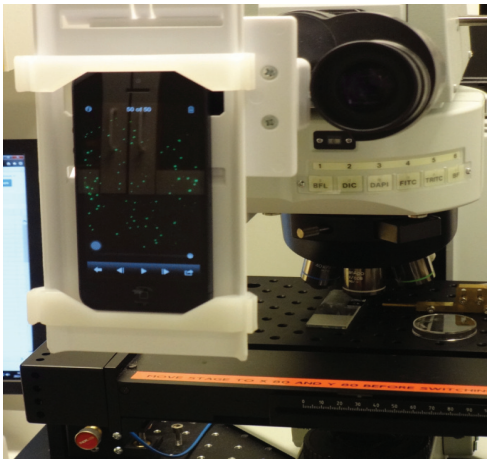

Figure 3.6: *Picture of how the mobile phone was mounted onto the microscope ocular in order to record the binding of gold particles.*

### 3.2.4 Analysis

One aim of the experiment was to analyse how the signal-to-noise ratio and the contrast vary depending on the exposure time, gain and laser input power used when recording the pictures. To do so, the chip was washed after use by dilution in water, leaving the attached particles on the chip surface but no other particles able to attach, see figure 3.7. From there, snapshots were taken of even parts of the waveguide surface. These snapshots were later used by the program ImageJ to evaluate scattering intensity and size distribution.

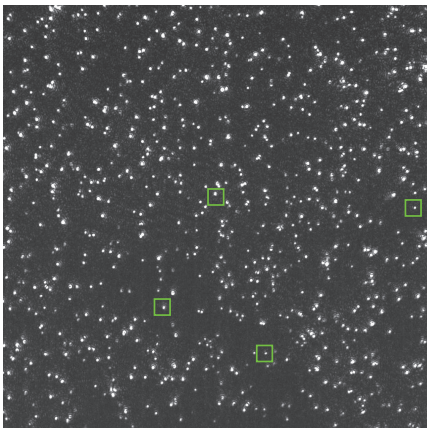

Figure 3.7: *Here, gold particles of diameter 65 nm have attached onto the waveguide surface. The four particles exhibited were later used for the determination of the dependence of laser power, exposure time and gain on the signal-to-noise ratio and the contrast.*

## 3.3 Pre-study for particle size estimation by NTA and SEM

For all the measurements performed, it is of importance to know the size of the particles used. Therefore the particle sizes have been measured, which will be presented in this section. Unfortunately the particles used, which were expected to be around 10 nm i diameter, were too small to yield useful waveguide data. But the size distributions for the 20 nm, 30 nm and 65 nm particles are presented in figures 3.8 and 3.9.

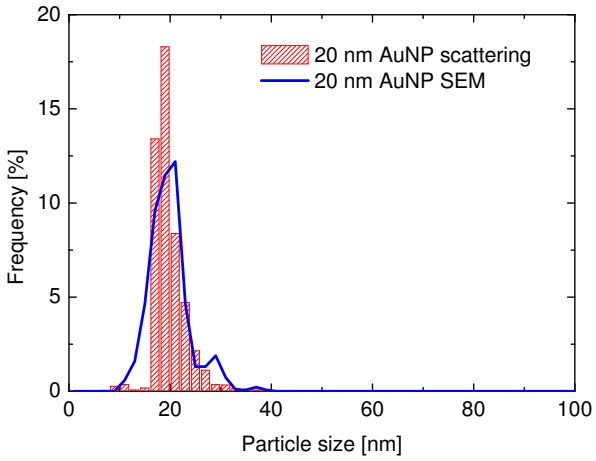


Figure 3.8: *Size distribution of the 20 nm sized gold particles. The solid line is a result of a SEM measurement while the histogram is scattering data measured with the waveguide system.*

In figure 3.8, the size distribution of the 20 nm gold particles is presented. The solid blue line is the size distribution made from some scanning electron microscope (SEM) pictures. The red coloured histogram in the back is a size distribution made from pictures acquired from the waveguide microscope (compare to figure 3.7). A horizontal adjustment of the waveguide histogram is made to fit the SEM distribution, since SEM is a very precise measuring technique.

A similar size distribution is also made for the 30 nm and 65 nm particles in figure 3.9. Instead of SEM, Nanoparticles Tracking Analysis (NTA) has been used. There has proved to be a small error with the NTA measurements. When comparing the size distributions to the very precise measuring technique SEM, the NTA adds around 10 nm to the particle sizes. Take this in consideration for figure 4.9. The solid blue lines represent the NTA size distribution and the red coloured histograms in the back are made from scattering statistics from the waveguide measurements. Also in this figure, the scattering histograms have been horizontally adjusted to fit the NTA data.

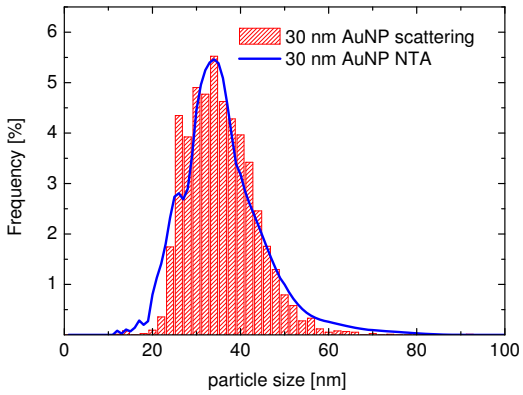


(a) *Size distribution of the 30 nm sized particles.*

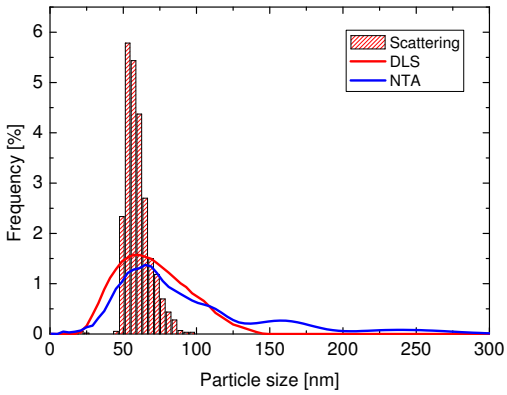


(b) *Size distribution of the 65 nm sized particles.*

Figure 3.9: *Size distribution of the 30 nm 65 nm sized gold particles. The solid lines are results of NTA measurements while the histograms are scattering data measured with the waveguide system. The NTA data has proved to display sizes roughly 10 nm too large. This is thought to stem from the fact the program used, NanoSight, measures the hydrodynamic size of the particles.*

# 4
# Results

In the following result section, results from the simulation session and from the experimental session will be presented. First the results acquired from Comsol, with simulation of the waveguide in two dimensions, are discribed. This was done to visualise how the electromagnetic field will distribute when introduced into the core layer of the waveguide. Afterwards, a comparison is made between Comsol simulations and theory of how gold nanoparticles scatter light. In the end of this chapter results from the experimental session are presented. These include how experimental parameters may be varied to optimise the results.

## 4.1 Simulations

One of the fundamental objectives of the simulations of this thesis was to see if the modal theory of section 2.2 could be recomposed in a numerical simulation program such as Comsol. This is done in the first subsection below.

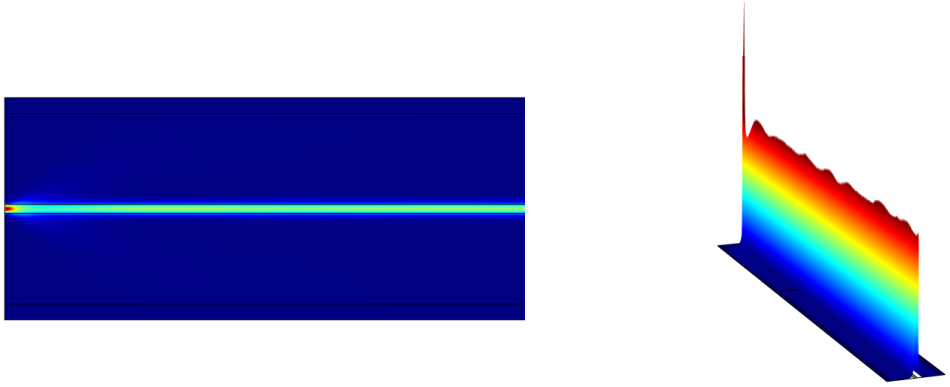

(a) *Two-dimensional representation of how the electromagnetic field is distributed inside the waveguide.*

(b) *Three-dimensional representation of the electromagnetic field inside the waveguide. The colour range is narrowed compared to figure (a).*

Figure 4.1: *Electric field norm squared. Red represents a strong field and blue represents a weak field. The thickness of the core layer is 400 nm. The thickness of the cytop layers are 4 µm. The left boundary of the core layer has been set to simulate a laser. It is attained by setting an incident monochromatic electric field as a boundary condition.*

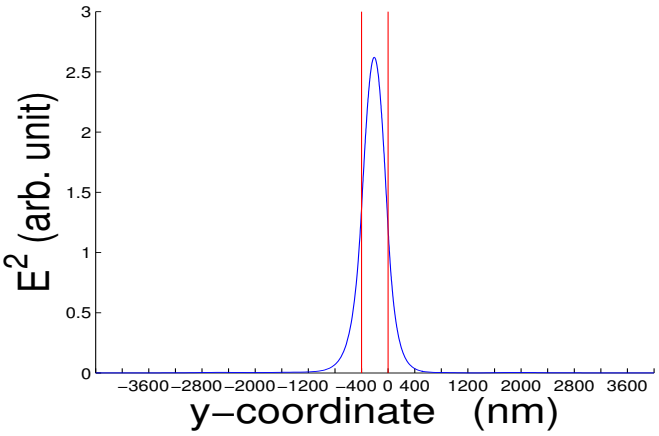


Figure 4.2: *A cross section of the simulated waveguide mode inside the SOG layer. The vertical red lines indicate the borders of the core layer. It can clearly be seen in this figure that there is an evanescent field outside the core layer.*

### 4.1.1 Field distribution inside the waveguide

The external electromagnetic field representing the laser light was set as a boundary condition on the left side of the core layer of the waveguide. The frequency of the field corresponds to the wavelength of 532 nm laser used during the experiments. Figure 4.1a is a stationary solution of the electromagnetic field's distribution inside the waveguide chip. The colours answer to the electrical field squared, $E^2$.

Another way to display the modal shape of the field and to be able to compare it to the theoretical field distribution mode is to look at it in cross section, which is done in figure 4.2. In that figure it can be seen how the simulated mode looks like. The vertical red lines indicate where the core layer of the waveguide is. Since the refractive indices of the core layer and the cladding layers lie very closely to each other, the field mode will also continue in evanescent tails in the cladding layers, which is visualised in the figure. The penetration depth is defined as how far into the cladding the field penetrates before its amplitude has dropped to $1/e^8$. For the kind of waveguide used in this thesis, this means a penetration depth of 237 nm. By studying figure 4.2 it is possible to determine the penetration depth to be 230 nm, which is sufficiently good.

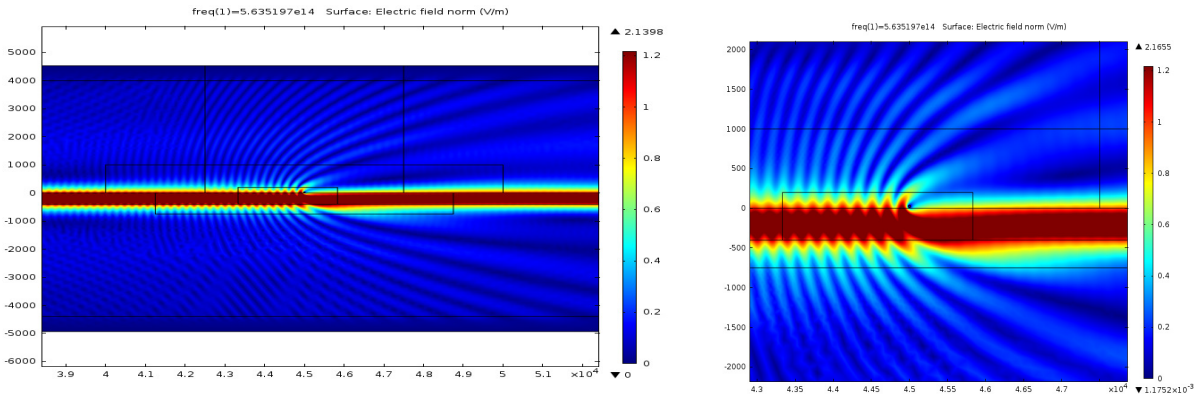


(a) *Figure of how the field behaves if there is a gold nanoparticle that has attached onto the surface of the waveguide.*

(b) *Zoom in around the gold particle.*

Figure 4.3: *Electric field norm. Red represents a strong field and blue represents a weak field. Thickness of core layer 400 nm. Thickness of cytop layers 4 µm. There's an incoming electric field incident from left into the channel.*

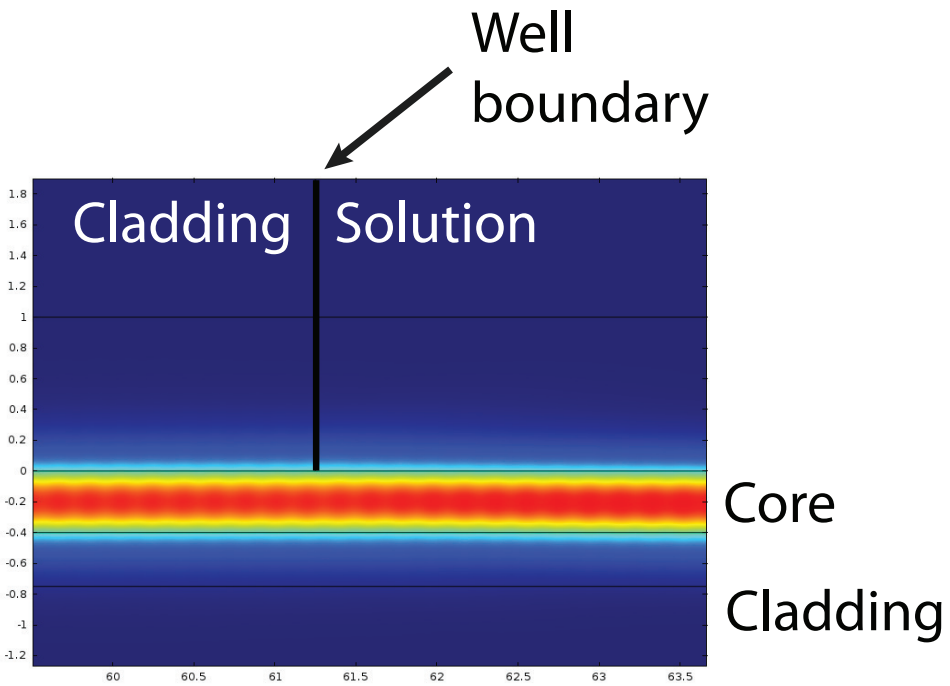


Figure 4.4: *Zoom-in of the electrical field simulation over the well border. Red colour indicates a strong electrical field and blue represents a weak field. There is no visible change of the field when passing the well boundary.*

Figure 4.3 shows the simulation where a gold particle of diameter 30 nm is put on the waveguide chip surface. The electric field seems to congest in front of the particle. The author has not been able to conclude anything qualitatively from these pictures although much work has been done to investigate the scattering further.

One interesting question was how the evanescent field changed over the boundary of the waveguide well. A simulation of this is made in figure 4.4. The figure shows a zoom-in of the evanescent field simulation. As can be seen, there is no visible change of the field on either side of the well boundary - just as desired. The cytop cladding is fabricated in such a way that its refractive index would match the one of water. Therefore there is no change in the evanescent field when passing from the cladding, across the well boundary and into the water solution of the well.

### 4.1.2 Scattering

As long as the simulated particle was situated in vacuum, the scattering simulations performed in Comsol agreed with theory. These results are presented in figure 4.5. The tendency is that forward scattering increases as the reduced size $q$ increases, as long as $q$ not exceeds unity.

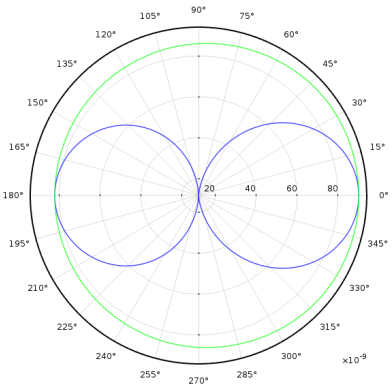

(a) *Simulation of scattering for a particle with a small q-value.*

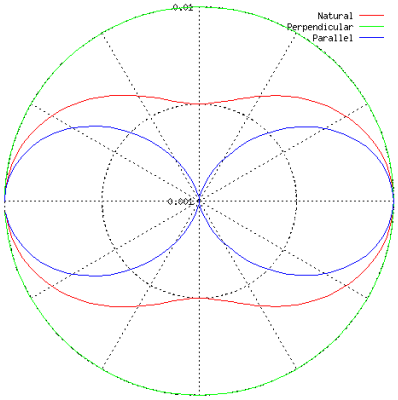


(b) *Theoretical scattering of a particle with a small q-value.*

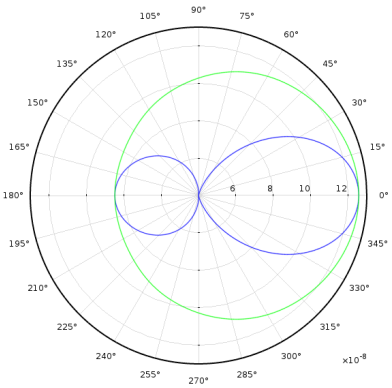

(c) *Simulation of scattering for a particle with a quite large q-value.*

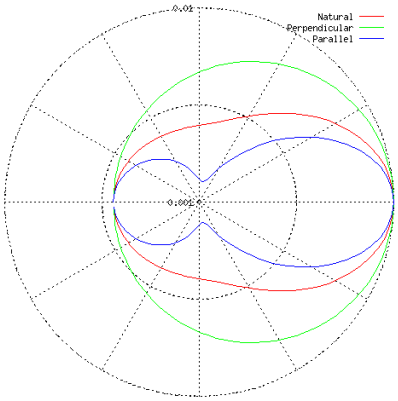


(d) *Theoretical scattering of a particle with a quite large q-value.*

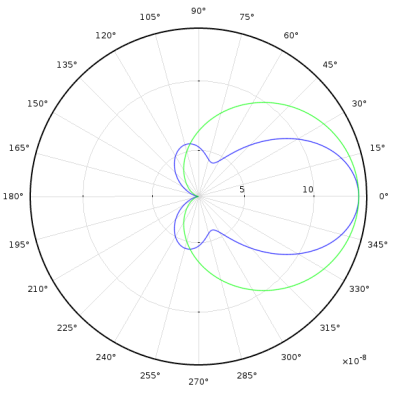

(e) *Simulation of scattering for a particle with a large q-value.*

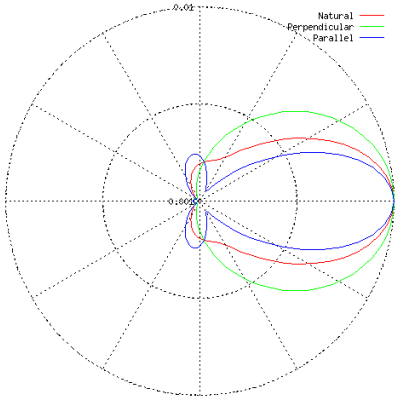


(f) *Theoretical scattering of a particle with a large q-value.*

Figure 4.5: *A comparison to the simulated shapes (to the left) and the theoretical shapes (to the right) of the scattering. The inner, blue line represents the parallel polarised light and the outer, green line represents the electric field polarised perpendicular to the scattering plane. The tendency is that for small values of q, the parallel polarised electric field will scatter both forward and backward, and for larger values of q, the scattering will be more and more directed forward. These simulations are made by a plane wave in vacuum.*

## 4.2 Experiments

The experimental part of the result section focuses on some of the questions raised during the experimental work. As the biology behind the measurements is well known, the questions regarding image analysis are the most crucial to answer. How do the particles scatter light as the laser power input varies? And how do the images behave when varying parameters like the exposure time and gain?

In figure 4.6, the intensity is plotted as a function of time when the particles are added to the analyte solution on top of the chip. Figure 4.6a displays the binding curve acquired by the microscope while figure 4.6b is acquired by the use of the mobile phone. The measurements were acquired simultaneously, but while Micro-Manager took one picture each second, O Snap took pictures with the mobile phone every five seconds.

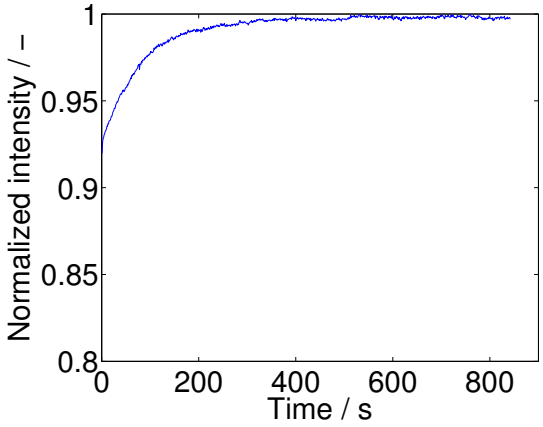


(a) *Microscope. One picture acquired each second.*

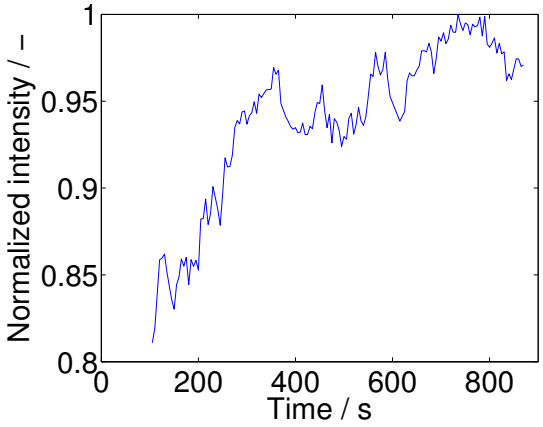


(b) *Mobile phone. One picture acquired every five seconds.*

Figure 4.6: *Binding curves for the microscope and for the mobile phone. The size of the particles used during this measure were size 65 nm. After about 200 seconds, a depletion layer has been formed and will decrease the rate in which the particles diffuses down to the surface.*

The shape of the binding curve of figure 4.6 is seemingly indicating that equilibrium is reached after a couple of minutes. But this is just an illusionary effect caused by limited mass transport. When the target molecules are introduced to the analyte solution, they start to diffuse and by chance they also reached the detectable region close to the waveguide surface. But the effect of figure 4.6 is due to a depletion layer close to the detectable region created by molecules bound to the surface. When a depletion layer has emerged in the bulk, the mass transfer rely purely on concentration gradient diffusion [14], making it a very slow process and it appears to be at an equilibrium, unless one continuously will mix. It is possible to avoid this problem by mixing the analyte solution with a pipette. But then the danger is that the equipment is unsettled and that the focus of the microscope is lost.

### 4.2.1 Measuring parameters

It has been clear during the measurements that the intensity doesn't increase strictly linear as a function of the laser power input. Therefore, it is interesting to look at how the parameters laser input power, exposure time and gain can be varied to optimise the signal-to-noise and contrast ratios. This is demonstrated in figures 4.7 and 4.8.

In the three parts of figure 4.7, the contrast is plotted as functions of laser input power (4.8a), exposure time (4.8b) and gain (4.8c). Contrast is computed as

$$Contrast = \frac{I_{max} - I_{back}}{I_{back}}\,, \tag{4.1}$$

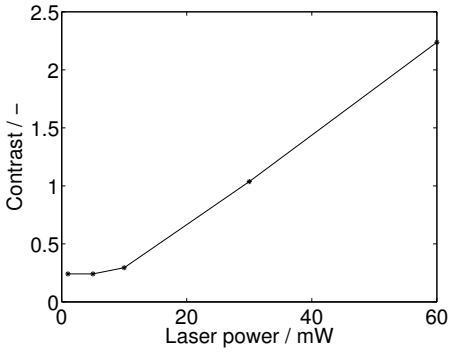


(a) *Contrast as a function of laser input power.*

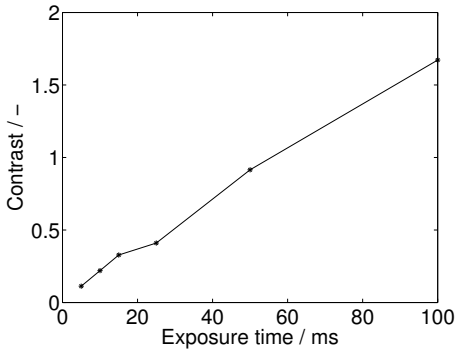


(b) *Contrast as a function of exposure time.*

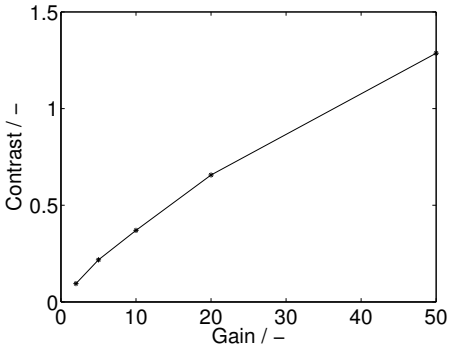


(c) *Contrast as a function of gain.*

Figure 4.7: *Measurements of how the contrast varies depending on the laser input power, the exposure time and the gain. When varying the laser input power, the exposure time was set to 10 ms and gain was set to 5. When varying the exposure time, the laser input power was set to 1 mW and gain was set to 5. When varying the gain, the laser input power was set to 1 mW and the exposure time was set to 10 ms.*

where $I_{max}$ is the top value of the signal and $I_{back}$ is a mean value of the background signal. Thus a high contrast is preferable. If the signal of everything detected would increase linearly with the parameters laser input power, exposure time and gain, the contrast would stay constant when varying these parameters. But, the signal is scattering from particles, which makes it non-linear relative e.g. laser input power. For laser input power, the signal-to-background ratio would increase with increasing power, which also can be seen in figure 4.7a. This is the case for the parameter exposure time as well. The longer time the measuring device has to acquire the signal, the higher contrast would be, see figure 4.7b. When it comes to gain, it is not as simple. Usually gain indicates how much each small part of the signal shall be magnified. In that case, the absolute value between the signal amplitude and the background would be unchanged. At the same time, both the signal and the background noise increases, making the ratio between the both decreasing. But on the other hand, as long as the signal stays within the dynamic range of the measuring device, the ratio may also stay unchanged. However, none of these explain the behaviour in figure 4.7c. Maybe it comes down to some underlying non-linearity of the measuring device.

In the three parts of figure 4.8, the signal-to-noise ratio (SNR) is plotted as functions of laser input power (4.8a), exposure time (4.8b) and gain (4.8c). SNR is defined as

$$SNR = \frac{I_{max} - I_{back}}{\sigma_{min}}\,, \tag{4.2}$$

where $I_{max}$ is the signal amplitude, $I_{back}$ is the mean value of the background and $\sigma_{min}$ is the fluctuation of the background signal divided by 5. That makes SNR a measure of how large the signal is compared to the background fluctuation. Therefore it is difficult to make predictions of how the SNR depends on

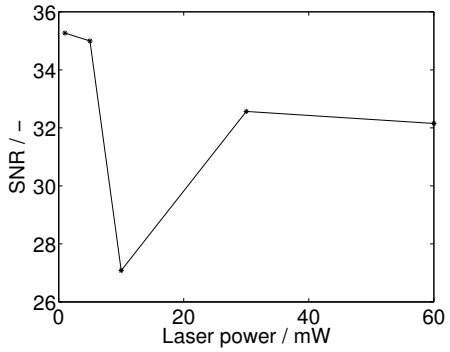


(a) *SNR as a function of laser input power.*

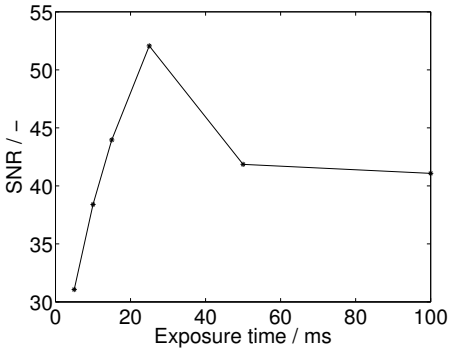


(b) *SNR as a function of exposure time.*

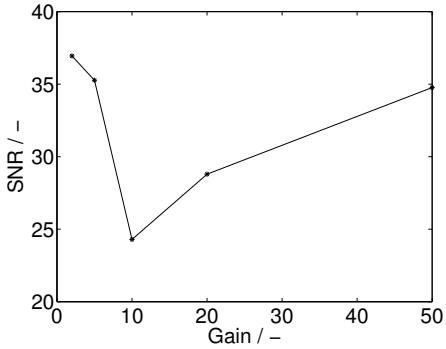


(c) *SNR as a function of gain.*

Figure 4.8: *Measurements of how SNR varies depending on the laser input power, the exposure time and the gain.*

laser input power. Figure 4.8a doesn't make it clearer. To be able to make better predictions and to rely on the results, a more comprehensive study has to be done with more data from different measurements. As long as the camera does not saturate, longer exposure times should result in a higher SNR. This also seems to be the case in the lower region of figure 4.8b, even though the measurement points for 50 ms and 100 ms makes it hard to draw any conclusions from that figure. As it comes to SNR dependence of gain, there probably is an optimum. Unfortunately the data making up figure 4.8c is too parsimonious because there are some indications that the optimum lays around a gain of 200 - 300.

### 4.2.2 Scattering

One aim of the experiments was to see if it is possible to measure two different sizes of particles from the same waveguide microscope picture. During experimental sessions, both 30 nm and 65 nm particles were immobilised on the waveguide surface. The program Origin was used by Agnarsson to make a size distribution of the particles on the surface. This is displayed in figure 4.9. The left peak of the distribution was horizontally adjusted to 30 nm, after determining the size of the 30 nm particles in section 3.3.

### 4.2.3 r-dependence of scattering

In section 2.4.1, the dependence of the particles' radii on the scattering is brought forward. There, it is stated that the scattering depends on the radius of the sphere as $r^6$. Is it possible to see this dependence in the pictures acquired from the waveguide microscope? For these measurements, gold particles of size 20 nm, 30 nm and 65 nm have been used. First of all, the data from figure 4.9 has been used in figure 4.10 to visualise the radial dependence. In the figure, the left peak for 30 nm particles has been kept fixed, while the right peak for the 65 nm particles has been adjusted as if the scattering had different

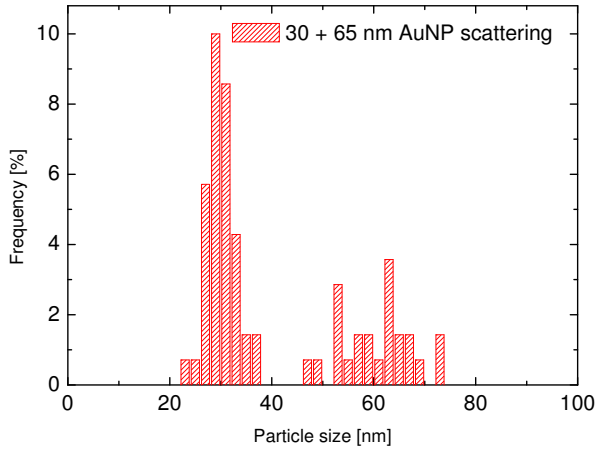


Figure 4.9: *Size distribution both 30 nm and 65 nm particles. The data was obtained by waveguide scattering measurement.*

radial dependencies. The figure shows how the size distribution would look like if the 65 nm particles would have scattered in a $r^4$, $r^5$, $r^6$, $r^7$ and $r^8$ manner compared to the 30 nm particles. Because the particles are 65 nm, the best distribution fit is made at $r^6$, which is in line with theory.

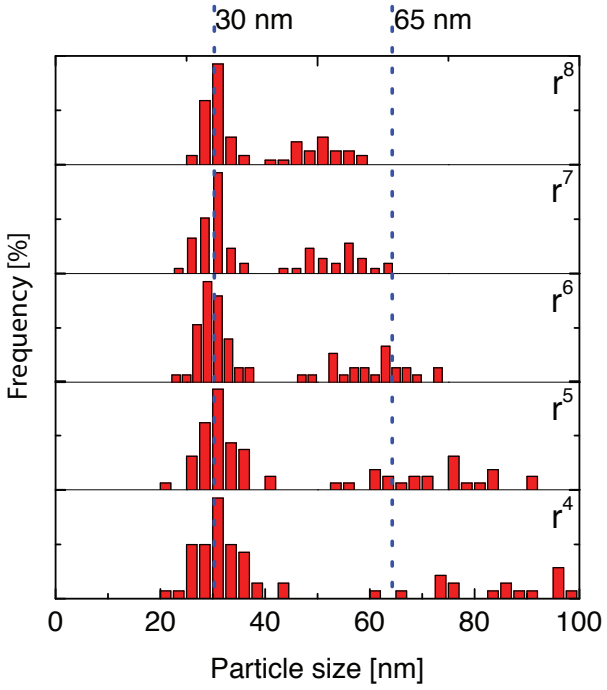


Figure 4.10: *Size distribution of 30 nm and 65 nm particles. The different parts of the picture show how the size distribution for the 65 nm particles would look like if the scattering intensity would be proportional to the $r^4$, $r^5$, $r^6$, $r^7$ and $r^8$, where $r$ represents the particle radius.*

With the $r^6$ dependence validated, it is interesting to see within which error margin these measurements lie. To find out about this, a Matlab script has been written to calculate the theoretical relation between the radius of the larger spheres and smaller spheres. The result is presented in figure 4.11.

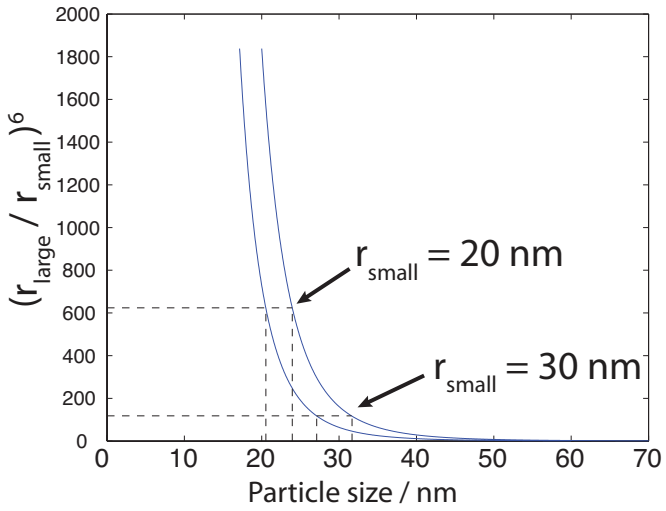


Figure 4.11: *Scattering relation of two measurements; one with 20 nm and 65 nm particles and one with 30 nm and 65 nm particles. The solid lines represent theoretical relations if the largest particles would have been 60 nm (left line) and 70 nm (right line), i.e. ±5 nm from their real size. The dashed lines represent the two scatter measurements and indicate that the smaller particles are sized between 20 nm and 24 nm and the larger particles are sized between 27 nm and 32 nm (real sizes are 20 nm and 30 nm). The scale on the y-axis originates from the $r^6$ relation where $r_{large}$ are the 65 nm sized particles.*

The data used is obtained from one measurement with 20 nm and 65 nm particles, and one measurement with 30 nm and 65 nm particles. The right solid line is the theoretical line for how the scatter intensity relation would be if the larger particles were sized 70 nm. Equivalently, the left solid line represents the relation had the larger particles been 60 nm. In such way, the two solid line represent an error margin of ±5 nm of the bigger particles. The horizontal dashed lines display the measured scatter relation between the 20 nm and 65 nm particles (top) and between the 30 nm and 65 nm particles (bottom). The positions at which the horizontal dashed lines and the solid lines intercept would then represent how large the smaller particles would be if the scatter measuring technique is good. The measurement for the relation between the 20 nm and 65 nm particles specifies that the size of the smaller particles lies between 20 and 24 nm. The corresponding measurement for the 30 nm particles specifies that the particles are sized between 27 and 32 nm. These results indicate that the method for size determination of gold nanoparticles is promising. Both particle sizes lies within the error margin, although the value for the 20 nm particles lie on the edge of the margin.

# 5
# Discussion

This chapter will contemplate and discuss the different parts of the thesis work. How were the methods used? Did the results agree with the theory? First, the methods used will be discussed and further down the results will be discussed. Each subsection will dig a bit deeper into the specific steps of the work.

## 5.1 Methods

When first introduced to the challenges and problems within the area of biological physics, I felt thrilled at seeing all the possibilities and unexplored territory. This has not changed during this working period, rather the reverse - especially with the possibility to work with biology but with a physical approach. But doing research is also about looking for, and finding, good working methods.

### 5.1.1 Simulations

When deciding the content of the thesis, I was sure that I wanted to do a combination of theoretical and practical work. And I thought it would be fun to perform both simulations and experimental work. The fact that the simulations were made in Comsol was mainly due to the fact that I already knew the program a bit. But also because it has a huge potential within different parts of physics.

Now afterwards, I probably would have choose another program for the scattering simulations if I would redo the thesis. Maybe I would have worked more with Matlab or Mathematica. Comsol worked fine for two-dimensional simulations. But as the models grew bigger, and especially when modelling in three dimensions, they often became too time consuming and the program crashed a couple of times during the process. I used version 4.3a, but version 4.3b was released during the course of this thesis with a new module for wave optics which, probably, would have worked smoother than the electromagnetic waves module which was used.

#### Waveguide mode

As far as the two-dimensional simulations were concerned though, Comsol worked quite fine. There were some doubtful numerical effects, but as a whole the two-dimensional simulations agreed with theory. When comparing the mode of figure 4.2 to mode D of figure 2.2, there is nothing indicating that the simulations wouldn't be true. Also, with only a difference of 7 nm between the theoretical prediction and the simulation outcome, the penetration depth should indicate a successful simulation.

The electrical field of the simulated laser was set as a boundary condition at the left short side of the core layer in the simulation model. Maybe it had been better if it had been introduced as a Gaussian shaped wave front on the whole left side to shorten the distance of mode setting. I did try to introduce the field sine shaped, but only on the left short side of the core layer, and it made no difference in the mode shape inside the core layer. Though it may have helped to get a smoother exponentially decaying field in the cladding layers. In the final simulations, the field fluctuates a bit in its evanescent parts. This

is not in complete accordance to theory, but it probably originates from some reflections in the outer boundaries of the waveguide. It is also probable that there is some kind of numerical error behind this problem, but I have been unable to find the source of it.

#### Scattering

The original idea was to use the modal field obtained in the two-dimensional model as background field in the three-dimensional scattering simulation. After a lot of tries and hard work, I had to abandon this idea. Comsol is built in a way that it is not possible to set any field as a background field. The background field has to be a solution to the geometry. For the case where the incident wave travels in vacuum it works fine as can be seen in figure 4.5. But when I tried to simulate the gold nanoparticle in water, the geometry didn't allow propagation of an evanescent field that would scatter on the particle.

Before I realised the problem of incompatible geometries, I worked out simulation methods for mimic not only different wavelengths and particle sizes, but also how vesicles would scatter light. Unfortunately these simulations had to be discarded.

### 5.1.2 Experiments

I think the method of using an evanescent waveguide field that scatters on nanoparticles is great. Once the waveguide chips are manufactured, the equipment is easy to learn how to use and doesn't require hazardous preparations. Furthermore is the big advantage, as already said, that no fluorophores or biologically attached labels that may influence the measurements are needed. On one hand, gold nanoparticles will never stop scattering, as may be the eventual case of fluorophores. But on the other hand, the intensity of the scatter will go down as the particle concentration increases. This phenomenon needs to be qualitatively and quantitatively investigated. It originates from the fact that the gold particles not only scatter the light, but also absorb fair amounts of it. This was brought forward briefly in section 2.4.1. It is also stated in that section that absorption is more important than scattering for gold particles smaller than around 150 nm. How advantage could be taken with respect to this fact is a question that has no answer in this thesis, but there surely is plenty to write about it. But, as a measure, Jain [11] writes that gold particles of 80 nm give off light that is five orders of magnitude stronger than strong fluorophores, which indicates that the method of scatter measurements still should be considered as a valid method even for particles smaller than 100 nm.

## 5.2 Results

The results obtained are described. First the simulation results and then the experimental results will be discussed.

### 5.2.1 Simulation

It would have been really interesting to see how the field would scatter, had the three-dimensional model been compatible with the background field acquired in the two-dimensional model. Then parameters like particle radius, wavelength and the particles distance from the surface would have been varied. This idea ended with the geometry not being compatible with the physically electric field.

It can be seen in figure 4.1 that the electric field tends to decrease just after entering the waveguide and spread out to finally disappear. This is probably due to the fact that higher modes are not compatible withe this geometry of the waveguide, and they wear off shortly after entering the waveguide. Some of them can be recalled in section 2.2.1 as air radiation modes.

As can be seen in figure 4.5, the tendency is the same for the simulated scattered field as theory predicts. The larger the particle is in comparison to the wavelength, i.e. for larger $q$-values, the tendency is to get more and more forward scattering. This is often referred to as the Mie effect [6]. When the particle becomes too large compared to the wavelength, Rayleigh's theory no longer holds and the light will rather reflect on the particles, i.e. backscatter [6]. As mentioned in section 2.4.3, multiple scattering lobes emerges

as $q$ exceeds unity. This effect was also identified in the simulations. But, since the simulations only were qualitative measures, I didn't add these results to the result section. Theoretically [6], the only difference between scattering in vacuum and in water arises because of the shortening of wavelength as the light travels in a thicker medium. This effect was not obtained during the simulation session. The scattering reconstruction work out in accordance with theory only in the case where the wave travelled in vacuum, and not in water.

Figure 4.3 shows how the electromagnetic energy in the light mode is influenced by a 30 nm gold particle on the waveguide surface. Since the simulation is made in two dimensions, the circular gold particle in reality simulates a gold rod that reaches into, and out from, the plane of drawing. It is really hard to draw any conclusions from this figure. Maybe it could be useful to calculate the Poynting vector to see where the energy flux is directed.

### 5.2.2 Experiments

When performing the experiments, the gold nanoparticles were dissolved in an aqueous solution. That is why the cytop cladding layers are fabricated to match the refractive index of water. In that way, the evanescent field will also continue across the well boundary. The aim of figure 4.4 is to visualise this. The distribution of the electrical field is the same on both sides of the well boundary.

The gold nanoparticles attach to the surface and stay there due to electrostatic interactions. Sometimes during the experiments there were problems with getting the particles to attach and to stay on the surface. This effect probably derive from problems with the electrostatic interactions between the particles and the surface. As written in section 4.2, there is a problem with the mixing and mass transport in the analyte solution. When a solution of citrate ions was added to it, the repulsive electrostatic interactions decreased and much more nanoparticles landed on the surface. This was done only in the experiments where it seemed to be a problem with the charge of the surface or the nanoparticles.

When working with the preparation of the waveguide chips, I participated in the birth of a new routine when silanising the surface. This silanisation technique is described in 3.2.1 and imply that silanes are evaporated onto the waveguide chip. Previous, the silanes were either mixed with methanol and pipetted directly onto the surface of the chip, or they were evaporated onto the chip after being mixed with liquid paraffin. The paraffin made the solution less volatile, but at the same time, more dust particles also got stuck onto the chip surface, making it less suitable for measurements.

During the measurement sessions, I had to treat the problem of a defect related to the waveguide chip installation. If the laser fibre wasn't aligned perfectly, reappearing stripes turned up in the measurements. This is thought to originate from the thickness of the SOG layer of the chip, or maybe the angle with which the light enters into the waveguide. Sometimes it was possible to tune away by adjust the laser connection.

#### Size distributions

The reason for the size distribution figures 3.8 and 3.9 being presented in the method chapter instead of in the results chapter is that they belong to characterisation of the material used. It in more difficult to book the scanning electron microscope than it is to book the Nanosight device. Therefore only SEM measurements are performed on the 20 nm sized particles. Otherwise, SEM is a more reliable technique for size determination. When measure size distributions with NTA it is has proved that Nanosight tend to add circa 10 nm to the particle diameter. This is probably due to the fact that Nanosight measure the hydrodynamic size of the particles, i.e. the size of both particles and the water bound to them. The water that is bound to each particle makes the particle move a wee bit slower, misleading the measuring device to believe that the particles are larger than they actually are. Nanosight uses the theory of Stoke and Einstein to relate the diffusivity to particle size. So when particles bind water slowing them down, the measured sizes does not accurately agree with the actual particle sizes. It is difficult to know how much water each type of particle bind, making the error margin larger for NTA measurements than for SEM measurements.

### Radial dependence

Based on the size distribution measurements, figure 4.10 and figure 4.11, I have drawn the conclusion that it is possible to make good relative particle size estimations by means scattering measurements. Theory predicts that the scattering intensity increases proportional to the sixth power of the particle radius. By implementing this relation, it is possible to determine the relative size of two different monodispersed particle groups. So, if one of these particle sizes is used as a reference size (as e.g. the 65 nm particles in figure 4.11), it should be possible to fairly certain determine the size of the other particles. This conclusions is drawn from only a few measurements, so to validate it, more of these measurements and calculations have to be made.

# 6
# Conclusion and outlook

The conclusions of the project will be presented in this chapter, as well as suggestions of future work possible within this area of research. In the first part of the thesis a theoretical background was presented, raising the questions whether it is possible in any way to deduce the theory by means of either simulations, experiments or both.

With a two-dimensional simulation of a three-layer planar optical waveguide, I have recreated the by theory presupposed fundamental mode. The fundamental mode is supported by the waveguide resulting in an attenuating evanescent field in the cladding layers with a penetration depth of 230 nm.

My three-dimensional model for predicting the scattering of gold nanoparticles wasn't as successful. The tendencies of the simulated scattered field corresponded to the trends found in the theoretical research, but only to the extent of scattering in vacuum. It was found that scattering for small, spherical particles is symmetric in the plane of scattering. But for larger particles, the scattering becomes more pronounced in the forward direction and for particles with the reduced size parameter $q$ surpassing unity, a large number of scattering lobes will appear. All of these behaviours coincide with theory.

The theoretical part of the report is followed by a description of the methods used in this thesis. Among the many different methods and programs used, some have worked better than others. As concluded above, the simulations made in Comsol worked fine for the two-dimensional case. They also worked well for the part of the three-dimensional simulations with scattering in vacuum, but neither for water nor other solution mediums.

When it comes to using the evanescent waveguide chip as a method for single nanoparticle detection, the conclusion is that it has everything to become a great method. The method has to be investigated more thoroughly and be more automated before being a real option on the market. But, as it is demonstrated in this thesis, particles of just a few tens of nanometres can be seen with the simple setup of a mobile phone placed in front of the microscope's ocular.

The best method for functionalising the waveguide surface was shown to be evaporation of the silanes onto the surface, but it is harder to tell which settings are the best when it comes to optimise the performance of the waveguide with respect to which laser input power, which exposure time and what gain should be used. As a technique for determining the size distribution of the particles, SEM was superior in comparison to NTA. NTA was a good tool to measure the distribution of the particles, but to determine the actual size for the peak of the distribution curve, SEM together with ImageJ was a more precise method. When one knows the size of a monodispersed collection of gold nanoparticles immobilised on the waveguide surface, it is possible to determine the size of another collection of monodispersed gold nanoparticles by means of calculations using the fact that scattering depends on the sphere radius $R$, as $R^6$.

When it comes to prospective outlooks, I think the evanescent waveguide technique has a bright future as a biomedical detection method. Development of work that can be done to improve the technique is ongoing all the time. Experimental parameters are tested every week in the bio-labs in the department of biological physics at Chalmers University of Technology. Examples of experimental parameters being tested could for instance be how to best use the plasma cleaner, how to manufacture, handle and transport the waveguide chips or how to align the laser fibre under the microscope. It would also be interesting to

see how the signal attenuates along the waveguide as a function of the concentration of gold particles. Hopefully in the time to come, a good technique for medical diagnose can be developed using the optical waveguide.

If I was to reappraise the method for simulation, I would have used a computational program like Matlab or Mathematica instead of Comsol to evaluate the scattering. A suggestion is to look at e.g. Matzler,[13], or Schafer,[17] for Mie calculations in Matlab. Probably a Comsol model could be developed to make the simulations work out fine. If such a program will be developed, it would be very interesting to see if different kinds of fields could be assigned as background fields for simulation of scattering. Then one could make predictions of how a spherical particle would scatter depending on e.g. the penetration depth or the thickness of the core layer or which ambient medium is present. Hopefully it would be possible to combine the two simulation models to take the modal field of the two-dimensional model and use it as background field in the three-dimensional model. Another exciting prospect for simulations is to see how a dielectric sphere would scatter incident light. The dielectric sphere could represent a single- or multi laminar vesicle and it would be interesting to see how the scattering would change upon protein- or fluorophore absorption.

# Bibliography


[1] Björn Agnarsson. *Symmetric Evanescent-Wave Platform for Optical Excitation and Sensing in Aqueous Solutions*. PhD thesis, University of Iceland, 2010.

[2] Mohammadreza Alizadehheidari. *Waveguide-based TIRFM for Diagnostic Applications*. PhD thesis, Chalmers University of Technology, 2012.

[3] Peter J. Bevelacqua. Maxwell's Equations.

[4] Abhijit Biswas, Tao Wang, and Alexandru S Biris. Single metal nanoparticle spectroscopy: optical characterization of individual nanosystems for biomedical applications. *Nanoscale*, 2:1560–1572, 2010.

[5] C F Bohren and D R Huffman. *Absorption and scattering of light by small particles*, volume 1. Wiley, 1983.

[6] M Born and E Wolf. *Principles of optics: electromagnetic theory of propagation, interference ...*, volume 1. Camebridge University Press, Camebridge, seventh (e edition, 1999.

[7] D. Deirmendjian. *Electromagnetic Scattering on Spherical Polydispersions*. American Elsevier, New York, 1969.

[8] H C Van De Hulst. *Light Scattering by Small Particles*, volume 80. Dover Publications, Inc., New York, 1957.

[9] Robert G. Hunsperger. *Integrated optics*, volume 42. Springer, Newark, sixth edition, September 2004.

[10] John David Jackson. *Classical Electrodynamics*. Wiley, New York, third edition, 1999.

[11] Prashant K Jain, Kyeong Seok Lee, Ivan H El-Sayed, and Mostafa A El-Sayed. Calculated absorption and scattering properties of gold nanoparticles of different size, shape, and composition: applications in biological imaging and biomedicine. *The Journal of Physical Chemistry B*, 110:7238–7248, 2006.

[12] Christoph Langhammer, Bengt Kasemo, and Igor Zorić. Absorption and scattering of light by Pt, Pd, Ag, and Au nanodisks: absolute cross sections and branching ratios. *The Journal of chemical physics*, 126:194702, 2007.

[13] Christian Mätzler. MATLAB Functions for Mie Scattering and Absorption. *IAP Res Rep*, 2002-08:1139–1151, 2002.

[14] Franscensco Mazzotta. *Advanced Nanofabrication for Novel Plasmonic Biosensors*. PhD thesis, Chalmers University of Technology, 2012.

[15] Carl Nordling and Jonny Österman. *Physics Handbook for Science and Engineering*. Studentlitteratur, Lund, eighth edition, 2006.

[16] Katsunari Okamoto. *Fundamentals of Optical Waveguides*. Academic Press, 2006.

[17] Jan-Patrick Schäfer, Siu-Chun Lee, and A. Kienle. Calculation of the near fields for the scattering of electromagnetic waves by multiple infinite cylinders at perpendicular incidence. *Journal of Quantitative Spectroscopy and Radiative Transfer*, 113(16):2113–2123, November 2012.

[18] M A Van Dijk, A L Tchebotareva, M Orrit, M Lippitz, S Berciaud, D Lasne, L Cognet, and B Lounis. Absorption and scattering microscopy of single metal nanoparticles. *Physical Chemistry Chemical Physics*, 8:3486–3495, 2006.

[19] Meindert A Van Dijk, Markus Lippitz, and Michel Orrit. Far-field optical microscopy of single metal nanoparticles. *Accounts of Chemical Research*, 38:594–601, 2005.

# A
# Comsol procedures

## A.1 Two-dimensional model

### A.1.1 Model

Choose 2D.
Select module Radio Frequency → Electromagnetic Waves, Frequency Domain (emw).
Select Preset Studies → Frequency Domain.

Choose Global Definitions > Parameters.
Fill in the values of table A.1

Table A.1: Global parameters for the two-dimensional model

| Name | Expression | Description |
|---|---|---|
| length | 150 [µm] | Length of waveguide |
| lambda | 532 [nm] | Wavelength |
| heighttop | 4 [µm] | Thickness of upper cytop layer |
| heightbot | 4 [µm] | Thickness of lower cytop layer |
| channel | 0.4 [µm] | Thickness of channel |
| d | 10 [nm] | Distance from channel surface |
| well | 10 [µm] | Width of well |
| r0 | 15 [nm] | Radius of sphere |

### A.1.2 Geometry

The data of table A.2 will generate the geometry shown in figure A.1.

### A.1.3 Materials

All the domains are defined by three properties relevant for the emw-module, namely the relative permeability, the relative permittivity and the electrical conductivity. The values for these properties are stated in table A.3.

Table A.2: Geometries for the two-dimensional model

| Type | Name | Width | Height | Position (Base: Corner) |
|---|---|---|---|---|
| Rectangle | Cytop | length | heighttop | x=0; y=0 |
| Rectangle | Channel | length | channel | x=0; y=-channel |
| Rectangle | Cytopbot | length | heightbot | x=-heightbot; y=-channel |
| Rectangle | Well | well | heighttop | x=length×7/10; y=0 |
| Rectangle | MeshTop | length/8 | 1[µm] | x=length×67/100; y=0 |
| Rectangle | Meshbot | length/10 | 0.75[µm] | x=length×68/100; y=-0.75[µm] |
| Rectangle | InWell | well/2 | 0.2[µm]+channel | x=length×7/10+well/4; y=- channel |
| Rectangle | PMLtopl | length | labmda | x=0; y=heighttop |
| Rectangle | PMLbot | length | lambda | x=0; y=-heightbot-channel-lambda |
| Rectangle | Welltop | well | lambda | x=length×7/10; y=heighttop |

| Type | Name | Radius | Position (Base:Corner) |
|---|---|---|---|
| Circle | Gold1 | r0 | x=length×7/10+well/2; y=d+r0 |

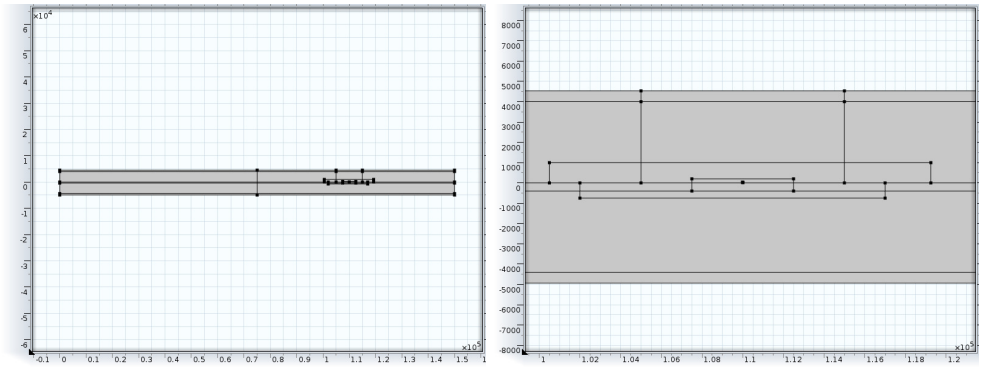

(a) *The whole structure of the two-dimensional model.* (b) *Zoom in around the well of the two-dimensional structure.*

Figure A.1: *The two-dimensional geometry.*

Table A.3: Material properties for the two-dimensional model

| Domain | Material | Relative permeability | Relative permittivity | Electrical conductivity |
|---|---|---|---|---|
| Channel | SOG | 1 | 2.0164 | 0 |
| Top and bottom | Cytop | 1 | 1.7956 | 0 |
| Well | Solution | 1 | 1.7689 | 0 |
| Circle | Gold | 1 | -4.74+2.31i | 4.1E7 |

### A.1.4 Electromagnetic Waves, Frequency Domain

The equation solved is

$$\nabla \times \mu_r^{-1}(\nabla \times \mathbf{E}) - k_0^2(\varepsilon_r - \frac{j\sigma}{\omega\varepsilon_0})\mathbf{E} = 0 \tag{A.1}$$

In the settings section, choose 'Solve for: Full field'.

### A.1.5 Boundary Conditions

The default boundary condition is 'Perfect Electric Conductor' to all exterior boundaries. Add the boundary setting 'Scattering Boundary Condition'. Select the vertical exterior boundaries as well as to

the upper and lower horizontal boundaries.

Add the boundary setting 'Electric Field'. Select the left vertical boundary of the channel, se figure A.2. This will represent the laser that excites the waveguide. Define the entering electric field as in table A.4.

Table A.4: ElectricField

| x | y | z |
|---|---|---|
| 0 | 0 | 1.94 |

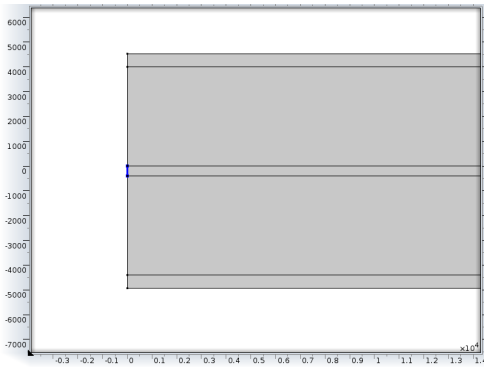

Figure A.2: *The left boundary of the channel has an electric field as a boundary condition.*

### A.1.6 Perfectly Matched Layer

Right-click 'Definitions' and choose 'Perfectly Matched Layer'. Select the topmost and bottommost domains/layers, se figure A.3. Set 'Geometry' to 'Cartesian'.

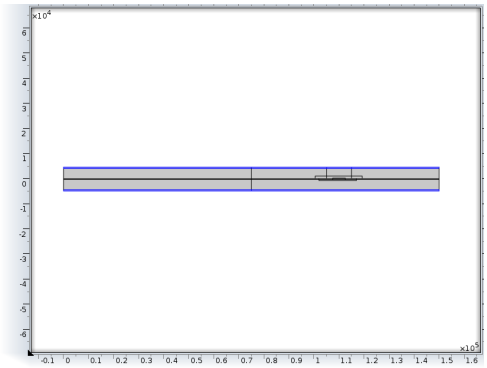

Figure A.3: *The topmost and bottommost domains are perfectly matched layers.*

### A.1.7 Mesh

Right-click 'Mesh' and add 'Free Triangular'. There you specify six different sizes as in table A.5.

### A.1.8 Run

In the frequency settings at 'Study 1 → 'Step 1: Frequency Domain', write frequency 'f0' Then run the program.

Table A.5: Mesh sizes

| Maximum element size | Domain |
|---|---|
| 250 [nm] | Left part of the waveguide except the channel. See figure A.4a |
| 150 [nm] | Cytop layers in right part of waveguide except well and channel. See figure A.4b |
| 50 [nm] | The channel and parts around the well. See figure A.4c |
| 25 [nm] | The well. See figure A.4d |
| 5 [nm] | Close to the gold particle. See figure A.4e |
| 2 [nm] | The gold particle. See figure A.4f |

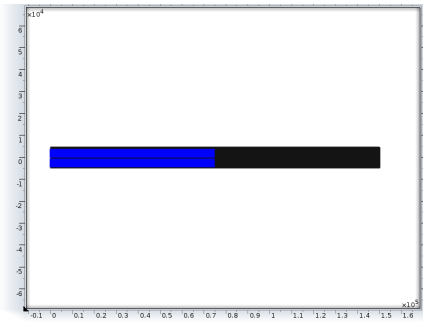

(a) *Domain where maximum element mesh size is 250 nm.*

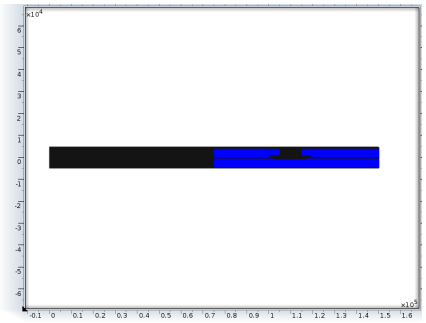

(b) *Domain where maximum element mesh size is 150 nm.*

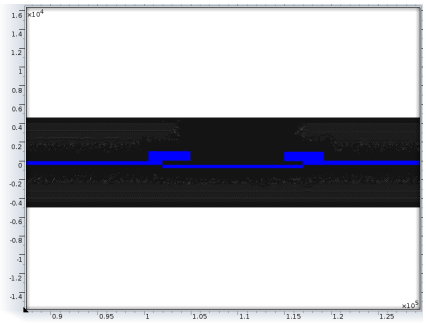

(c) *Domain where maximum element mesh size is 50 nm.*

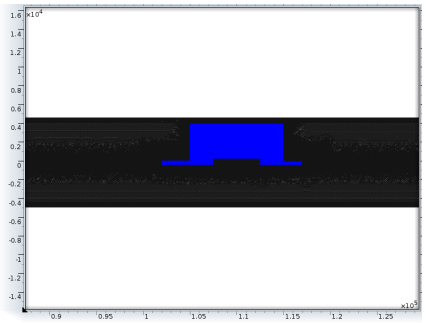

(d) *Domain where maximum element mesh size is 25 nm.*

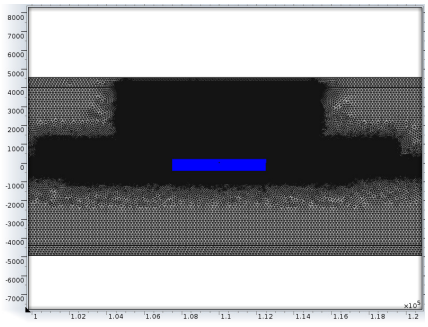

(e) *Domain where maximum element mesh size is 5 nm.*

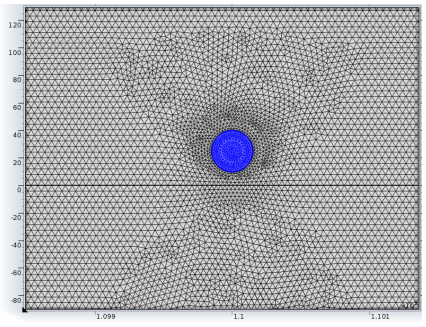

(f) *Domain where maximum element mesh size is 2 nm.*

Figure A.4: *Figures of the meshed geometry. The blue parts represent the domains for the respective subfigures. Figures (c) to (f) are zoomed in to visualise the meshing better.*

### A.1.9 Results

The default plot will show the electric field norm, se figure A.5.

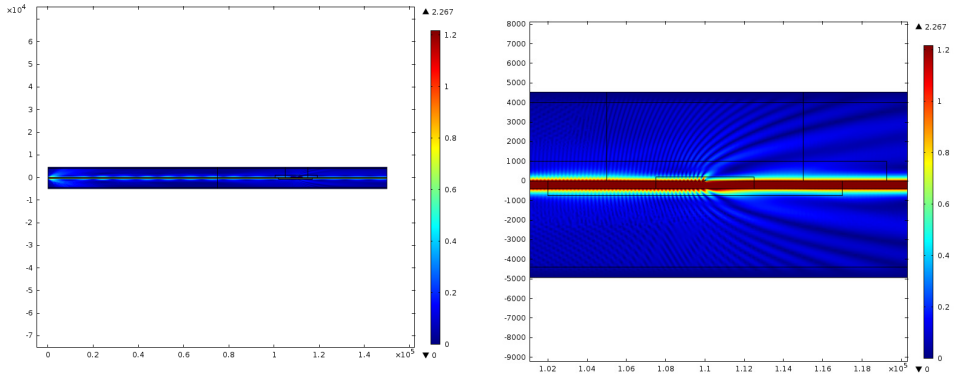

(a) *Electrical field norm of the whole structure.*

(b) *Zoom in around the well.*

Figure A.5: *Electric field norm of the two-dimensional model.*

Right-click 'Results' and add a '1D Plot Group'. Right-click 'Data Set' and click 'Cut Line 2D. Select the point of table A.6.

Table A.6: Points for line evaluation.

| $x_1$ | $x_2$ | $y_1$ | $y_2$ |
|---|---|---|---|
| length×72/100 | length×72/100 | heighttop | -heightbot-channel |

Right-click the 2D plot group and add 'Line Graph'. Select the Cut Line 2D and change the x-axis expression to 'y'. This will create a plot of the electric field norm as a function of the y component (across the waveguide) inside the well.

## A.2 Three-dimensional model

For the three-dimensional model, I have followed the Comsol model 'Optical Scattering Off of a Gold Nanosphere'.

### A.2.1 Model

Choose 3D
Select module Radio Frequency → Electromagnetic Waves, Frequency Domain (emw).
Select Preset Studies → Frequency Domain.

Choose Global Definitions → Parameters. Fill in the values of table A.7

Table A.7: Global parameters for the three-dimensional model

| Name | Expression | Description |
|---|---|---|
| r0 | 15 [nm] | Sphere radius |
| lambda | 532 [nm] | Wavelength |
| f0 | c_const/lambda | Frequency |
| t_sol | 1 [µm] | Thickness of solutions layer |
| t_pml | lambda/2 | Thickness of PML |
| t_max | lambda/6 | Maximum element size, solution |

### A.2.2 Geometry

Create a sphere with layers. The outermost layer represents the PMLs and the core represents the gold sphere. The middle layer is the solution domain. PML stands for Perfectly Matched Layer. In Comsol's users guide it is stated that PMLs are used for simulation of infinite domains. It further tells us that one has to stretch the virtual domains surrounding the physical region of interest into the complex plane by creating perfectly matched layers in order to absorb outgoing waves of a frequency-domain problem.

The preferred geometry is specified in table A.9.

Table A.8: Geometries for the three-dimensional model

| Type | Radius |
|---|---|
| Sphere | r0+t_sol+t_pml |

| Type | Width | Depth | Height |
|---|---|---|---|
| Block | 2×(r0+t_sol+t_pml) | (r0+t_sol+t_pml) | (r0+t_sol+t_pml) |

Specify the thickness of the sphere layers by expanding the 'Layers' section when creating the sphere to assign the outermost and middle layer to have thickness t_pml and t_sol, respective. And set the position (base: corner) of the block to be 0 for y and z and $-(r0 + t\_sol + t\_pml)$ as x-coordinate. Generate the quarter sphere by intersecting the two objects, see figure A.6.

### A.2.3 Materials

The outermost layer is made out of the built-in material properties for air. The other two domains are defined by three properties relevant for the emw-module, namely the relative permeability, the relative permittivity and the electrical conductivity.

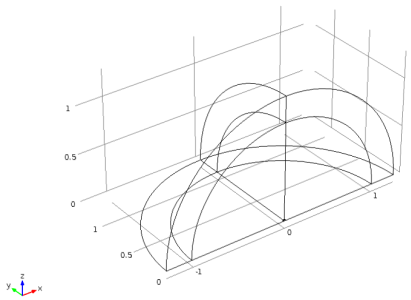

Figure A.6: *The geometry of the three-dimensional model.*

Table A.9: Material properties for the three-dimensional model

| Domain | Relative permeability | Relative permittivity | Electrical conductivity |
|---|---|---|---|
| Outermost | 1 | 1 | 0 |
| Middle | 1 | 1.7689 | 0 |
| Core | 1 | -4.74+2.31i | 4.1E7 |

### A.2.4 Electromagnetic Waves, Frequency Domain

Now set up the physics. You solve the model for the scattered field, so it needs background electric field (E-field) information.

The equation solved is

$$\nabla \times \mu_r^{-1}(\nabla \times \mathbf{E}) - k_0^2(\varepsilon_r - \frac{j\sigma}{\omega\varepsilon_0})\mathbf{E} = 0 \tag{A.2}$$

In the settings section, choose 'Solve for: Scattered field'. Specify the background field, E_b as 0 in x and y and to be exp(-j×emw.k0×x) in z, where emw.k0 is the wave number in free space.

### A.2.5 Wave Equation, Electric

Add the domain setting 'Wave Equation, Electric'. Select the gold domain.

In the 'Electric Displacement Field' section, choose Relative permittivity, $\varepsilon_r$, → user defined: -4.74+2.31×i, isotropic.

In the 'Magnetic field' section, choose Relative permeability, $\mu_r$, → user defined: 1, isotropic.

In the 'Conduction Current' section, choose Electrical conductivity, $\sigma$, → user defined: 4.1e7, isotropic.

### A.2.6 Scattering Boundary Condition

In the Model Builder window, right-click 'Electromagnetic Waves, Frequency Domain' and choose the boundary condition 'Scattering Boundary Condition'. Select the outermost boundaries, see figure A.7.

### A.2.7 Perfectly Matched Layer

Right-click 'Definitions' and choose 'Perfectly Matched Layer'. Select the outermost domain/layer. Set 'Geometry' to 'Spherical'.

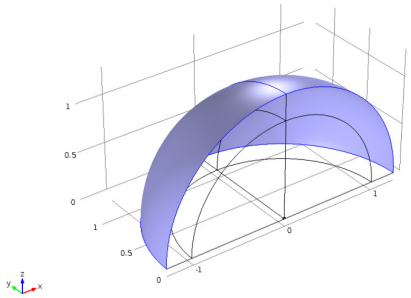

Figure A.7: *The outermost boundary is set as a scattering boundary condition.*

### A.2.8 Perfect Magnetic Conductor

The default boundary condition is perfectly electric conductor, which applies to all exterior boundaries, including the boundaries perpendicular to the background E-field polarisation. Set the boundaries in the x-z plane to perfect magnetic conduction, see figure A.8.

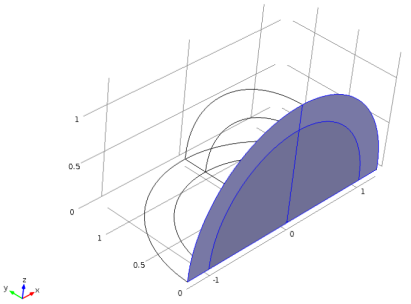

Figure A.8: *The boundaries in the x-y-plane is set as perfect magnetic conductor boundaries.*

### A.2.9 Far-Field Domain

Select the middle domain and set the domain setting 'Far-Field Domain', see figure A.9.

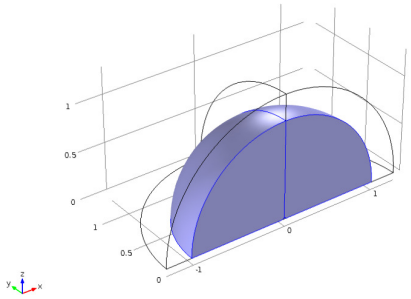

Figure A.9: *The middle layer is set as far-field domain.*

### A.2.10 Far-Field Calculation

Right-click 'Far-Field Domain' and click 'Far-Field Calculation'. Select the outer boundaries of the middle domain, see figure A.10.

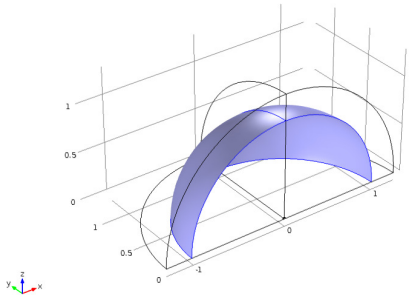

Figure A.10: *The outer boundary of the far-field domain is set as the boundary for far-field calculations.*

Select 'Symmetry in the y=0 plane' and choose 'Symmetry in E (PMC)' (PMC = Perfect Magnetic Conductor).

Select 'Symmetry in the z=0 plane' and choose 'Symmetry in H (PEC)' (PEC = Perfect Electric Conductor).

### A.2.11 Mesh

The maximum mesh size is at most 0.2 wavelengths in free space. To evaluate the gold sphere up to the accuracy level of the penetration depth, the Comsol model advises you to set the maximum element size inside the sphere around the half of the minimum skin depth over the frequency sweep range.

The core and middle layer are made up of free tetrahedrals with maximum element size 2 nm and h_max (lambda/6), respectively. The outermost layer is a 'Swept mesh', with number of elements fixed at 5, see figure A.11. Swept meshing is according to Comsol's blog a discretization technique of the geometry for specific types of geometries such as those with little or no variation in a specific direction. This type of meshing reduces the number of elements and the computational time in comparison to other (tetrahedral and triangular) meshes.

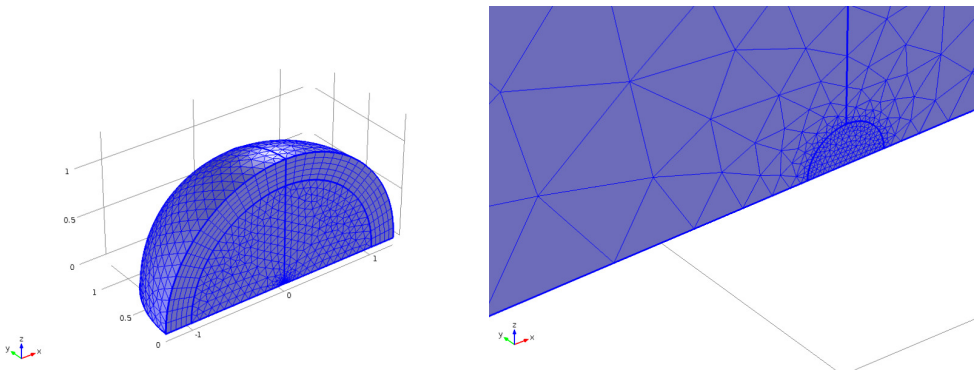

(a) *Mesh of the whole structure.*

(b) *Zoom in of the mesh around the gold particle.*

Figure A.11: *The mesh of the model. The outer perfectly matched layer is divided into five elements.*

### A.2.12 Run

In the frequency settings at 'Study 1' → 'Step 1: Frequency Domain', write frequency 'f0'.

Then run the program.

### A.2.13 Results

When the solution is computed, right-click 'Results' and add a '3D Plot Group' and a 'Polar Plot Group'.

### A.2.14 3D Plot Group

In the 3D plot group, add a surface plot and choose to view the x-y plane (because this represents the direction of the length of the waveguide, x, and the direction in which the detector is, y), see figure A.12.

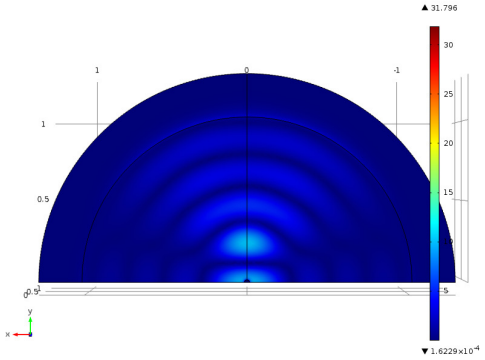


Figure A.12: *A 3D plot group showing the electric field norm.*

### A.2.15 Polar Plot Group

In the polar plot group, add a line graph plot by chosing 'Far Field', change the r-axis data to 'emw.normE' (electric field norm) and change the $\theta$ angle data to 'atan2(y,x)'.